ROTATIONAL AND THERMAL DYNAMICS OF NEUTRON STARS

by

Steven Curtis Price

A dissertation submitted in partial fulfillment
of the requirements for the degree

of

Doctor of Philosophy

in

Physics

MONTANA STATE UNIVERSITY
Bozeman, Montana

April 2012

APPROVAL

of a dissertation submitted by

Steven Curtis Price

This dissertation has been read by each member of the dissertation committee and has been found to be satisfactory regarding content, English usage, format, citations, bibliographic style, and consistency, and is ready for submission to The Graduate School.

Dr. Bennett Link

Approved for the Department of Physics

Dr. Richard J. Smith

Approved for The Graduate School

Dr. Carl A. Fox

STATEMENT OF PERMISSION TO USE

In presenting this dissertation in partial fulfillment of the requirements for a doctoral degree at Montana State University, I agree that the Library shall make it available to borrowers under rules of the Library. I further agree that copying of this dissertation is allowable only for scholarly purposes, consistent with "fair use" as prescribed in the U. S. Copyright Law. Requests for extensive copying or reproduction of this dissertation should be referred to Bell & Howell Information and Learning, 300 North Zeeb Road, Ann Arbor, Michigan 48106, to whom I have granted "the non-exclusive right to reproduce and distribute my dissertation in and from microform along with the non-exclusive right to reproduce and distribute my abstract in any format in whole or in part."

Steven Curtis Price

April, 2012

DEDICATION

This dissertation is dedicated to my daughter Nivienne Grace Price. May you find great enjoyment in exploring the beauty of this world, and discovering the unique place that God has for you in it.

ACKNOWLEDGEMENTS

I would like to thank my advisor, Dr. Bennett Link, for his guidance during my research. He is an excellent teacher and researcher, and his example has pushed me to strive for excellence in both areas. I also thank Dr. Steve Shore and Dr. Richard Epstein, who have shared their research projects and their love of physics with me. I acknowledge the Montana Space Grant Consortium for financial support during the time of this research.

I am especially grateful to my family. My mother and father, Linda and Richard Price have provided me with all the tools to succeed in life, and have encouraged me to question and discover the nature of the world around me. Their interest in and support of my research have been a constant source of motivation. No one deserves more thanks than my wife, who is a constant source of energy and strength for me. Her belief in me has carried me through times when my will has wavered.

God is my ultimate source of strength and purpose in life. I am thankful that he has guided me down this path, and given me the ability to complete this research endeavor.

TABLE OF CONTENTS

LIST OF TABLES

LIST OF FIGURES

Figure Page

LIST OF FIGURES - CONTINUED

LIST OF FIGURES - CONTINUED

LIST OF FIGURES - CONTINUED

LIST OF FIGURES - CONTINUED

LIST OF FIGURES - CONTINUED

Figure Page

ABSTRACT

This thesis explores the rotational and thermal dynamics of neutron stars. All neutron stars exhibit irregularities in their spin rates, which may be evidence of coupling between the solid crust and liquid components in the interior. We study short-time scale correlations in the stochastic variations in spin rate, *timing noise*, in 32 pulsars. Upon subtraction of low frequency wander, we find that in two stars a fluctuation in rotational phase at a given time is correlated with past fluctuations over a correlation time of $\sim 10-40$ d; over longer times, the fluctuations are uncorrelated. We interpret this result as the signature of a damped rotational mode in the star, excited by the noise process, and likely due to friction between the crust and interior liquid. In the second part of this thesis, we investigate the thermal and magnetic evolution of highly magnetized neutron stars, *magnetars*. We explore a thermo-resistive instability in the outer crusts of magnetars wherein a perturbation in temperature increases ohmic heating. We show that magnetars of characteristic age $\tau_{\rm age} \sim 10^4$ yr are unstable over timescales as short as days if strong current sheets are present in the outer crust. This instability could play an important role in the thermal and magnetic field evolution of highly magnetized neutron stars, and may be related to bursting activity in magnetars.

1. INTRODUCTION

1.1. History and Observation

Since their discovery in 1967, neutron stars have been used as astrophysical laboratories for testing theories of physics under the most extreme conditions in the universe. With approximately the same mass as the Sun and a radius of around 10 kilometers, the central density may be up to 10 times that of nuclear matter. The gravitational acceleration at the surface of such a compact object is $\sim 10^{11}$ times larger than on Earth. Magnetic fields may exceed 10^{14} G, seven orders of magnitude higher than can be produced in a terrestrial laboratory. Observations of neutron star behavior under such conditions may give insight into questions of fundamental physics from a wide variety of fields, including general relativity, ultra-high density matter, elementary particle physics, and stellar evolution.

The theory behind neutron stars began to develop soon after the discovery of the neutron itself in 1932. Baade and Zwicky theorized that a compact star made up of neutrons might might be produced in supernovae explosions (Baade & Zwicky 1934). It took over 30 for the first neutron star to be discovered in 1967 by Jocelyn Bell, part of a Cambridge team of scientists studying interplanetary scintillation (Hewish et al. 1968). Within a year, Gold (1968) proposed that a rotating neutron star approximately 10 km in radius possessing a magnetic field of $\sim 10^{12}$ G could explain the observed emission. He speculated that torque on the star from the rotating

magnetic field would cause a slowing down of the star's spin rate. This conjecture was soon verified by observations of the Crab pulsar, and the identification of pulsars as rotating neutron stars quickly became well established. Since the identification of the first neutron star, more than 2000 have been discovered. Their masses are calculated using binary systems to be between $1 - 2M_{\odot}$, and radii range from $8 - 15$ km, based on fits to observed spectra (see below). Rotation periods span a larger range, from ~ 1.4 ms to ~ 12 s. The precision of their rotation rate is astonishing - some pulsar rotation rates are known to 1 part in 10^{13}, making them comparable in precision to atomic clocks.

Like black holes and white dwarfs, neutron stars represent the final stage of evolution for main sequence stars. For the smallest stars ($M \lesssim 8M_{\odot}$), gravitational collapse occurs gradually as nuclear fusion ceases, resulting in a white dwarf. In these stellar remnants the gravitational force is balanced by electron degeneracy pressure. Stars more massive than $\gtrsim 25M_{\odot}$ end in supernova explosions and produce black holes. Neutron stars form in type II supernovae, enormously energetic explosions resulting from the collapse of intermediate mass stars ($8M_{\odot} \lesssim M \lesssim 25M_{\odot}$). During such a collapse, the temperature and pressure in deeper layers of the star increase rapidly, forming a neutron core. Once the core reaches a sufficient density the collapse is abruptly stopped due to the degeneracy pressure of the neutrons, sending out a shockwave which expels the outer layers of the star, leaving only the dense core.

After their formation, neutron stars may manifest themselves in a number of ways. The majority of neutron stars discovered to date, including the first, are seen from our vantage point in the universe as sources of pulsed radio emission. Charged particles are accelerated from the surface of the star at the polar caps by strong electric fields. A secondary plasma of electrons and positrons is formed above the polar caps through a cascade process and their acceleration around the magnetic field lines lead to radiation (Julian & Goldreich 1969). The polar cap region is small compared to the stellar radius, so emission leaves the star in a narrow beam. Rotation of the neutron star creates a "lighthouse effect", as the beam is observed once every rotation period. Pulsed emission has been observed in all wavelength bands of the electromagnetic spectrum, from radio frequencies through gamma rays. The dispersion of pulsed emission can be used to estimate the distance to pulsars, using multi-frequency observations of pulse arrival times, together with a model of the interstellar medium through which the pulse travels.

The fastest pulsars, known as millisecond pulsars are typically old ($10^9 - 10^{10}$ years), and have relatively weak magnetic fields (B $\sim 10^8 - 10^{10}$ G). These properties have led to their identification as "recycled" pulsars (Bhattacharya & van den Heuvel 1991). Recycling occurs as slowly rotating pulsars in binary systems accrete matter from companion stars, spinning up the star and decreasing the magnetic field strength.

Soft Gamma Repeaters (SGRs), and occasionally Anomolous X-ray Pulsars, reveal themselves through energetic explosions. These bursts produce emission in x-rays

and soft gamma rays. The energy released in burst events likely spans a continuum, but SGRs have exhibited peak luminosities $> 10^{47}\mathrm{erg\,s^{-1}}$, making them some of the most energetic explosions in the universe. The energetics of SGR bursts indicate that their sources are likely highly magnetized neutron stars, *magnetars*, possessing magnetic fields greater than 10^{14} G, inferred from measurements of P and $\dot{P}$. Relatively long rotation periods ($\gtrsim 2$ s) are common in these objects, due to rapid spin-down.

Other neutron stars reveal themselves to the observer only by quiescent thermal emission from the surface, usually in X-rays or optical frequencies (e.g., Pavlov & Zavlin 2003). Some thermal emitters are associated with supernova remnants, providing an accurate age estimate (e.g., Zavlin et al. 1999). These objects provide a unique opportunity to constrain theories of the cooling process of neutron stars, which is still uncertain (see, for example, Page et al. 2004). After an initial cooling period of around 100 years, the surface temperature will mirror the temperature of the core, but will be ~ 100 times lower. In this connection, observations of the surface temperature of thermal emitters with known ages can give important clues as to the nature of cooling processes in the core. We discuss neutron star temperature evolution further in Section 4.1.

A neutron star in a binary system may produce emission due to the accretion of matter from the companion star, such as the Hercules X-1 system (Brecher 1972).

Neutron stars which are actively accreting material are bright X-ray sources. Accretion can also lead to thermonuclear burning of the outer layers of the star, producing a flare of X-ray emission, a Type I X-ray burst (e.g., Bildsten 1998) .

Due to their small sizes and luminosities, the global properties of neutron stars are difficult to measure directly. A pulsar's age can be inferred in several ways: from associated supernova remnants, or from measurements of the spin period P and its derivative, $\dot{P}$. Under the assumption that the dipolar magnetic field radiates energy in vacuum, the characteristic age τ_c is

$$\tau_c = \frac{P}{2\dot{P}}. \tag{1.1}$$

The magnetic field strength can be inferred from the spin characteristics using similar assumptions. A dipolar magnetic field of strength B at the magnetic pole rotating with angular velocity Ω in vacuum radiates energy at a rate given by (Shapiro & Teukolsky 1983)

$$\dot{E} = -\frac{B^2 R^6 \Omega^4 \sin^2 \alpha}{6c^2}, \tag{1.2}$$

where R is the radius of the star, α is the angle between the magnetic dipole moment and the rotation axis, and c is the speed of light. The rotational energy of the star, $E_{rot} = I\Omega^2/2$, is the source of energy for the dipole radiation, where I is the moment of inertia of the star. The magnetic field strength B can be estimated once the spin parameters are known by equating the right hand side of Eq (1.2) with the time

derivative of E_{rot} . The magnetic field strength estimated using the dipole model is

$$B \simeq 3.2 \times 10^{19} \left(\frac{P\dot{P}}{s} \right)^{1/2}, \tag{1.3}$$

giving typical values in the range 10^9 to 10^{14} G.

Accurate measurements of neutron star masses have been made based on orbital parameters of neutron star binary systems. Several dozen systems with at least one neutron star have been analyzed, with the most precise measurements giving a narrow range for the neutron star mass, from $\sim 1.2 - 1.6 M_{sun}$ (Lattimer & Prakash 2005). In principle, once the mass and equation of state are known for a given neutron star, the radius can be calculated. However, the equation of state of high density matter is uncertain, leading to a wide range of mass-radius relationships which are not constrained by direct measurements. Radii can be inferred from quiescent emission spectra of low mass X-ray binaries (Guillot et al. 2011), or by fitting burst models to observations of thermonuclear flashes observed as type I X-ray bursts (Özel et al. 2012, Zamfir et al. 2012). Though these estimates are model dependent, they place upper limits on the neutron star radius of $\sim 9 - 13$ km.

1.2. Structure

A theoretical neutron star is commonly divided into several distinct parts: a thin atmosphere, a rigid crust and a liquid interior made up primarily of neutrons. A cross section of the current theoretical picture 1.4 M_{sun} neutron star is shown in Figure 1 . Near the surface the crust is made up of a lattice of iron-like nuclei surrounded by

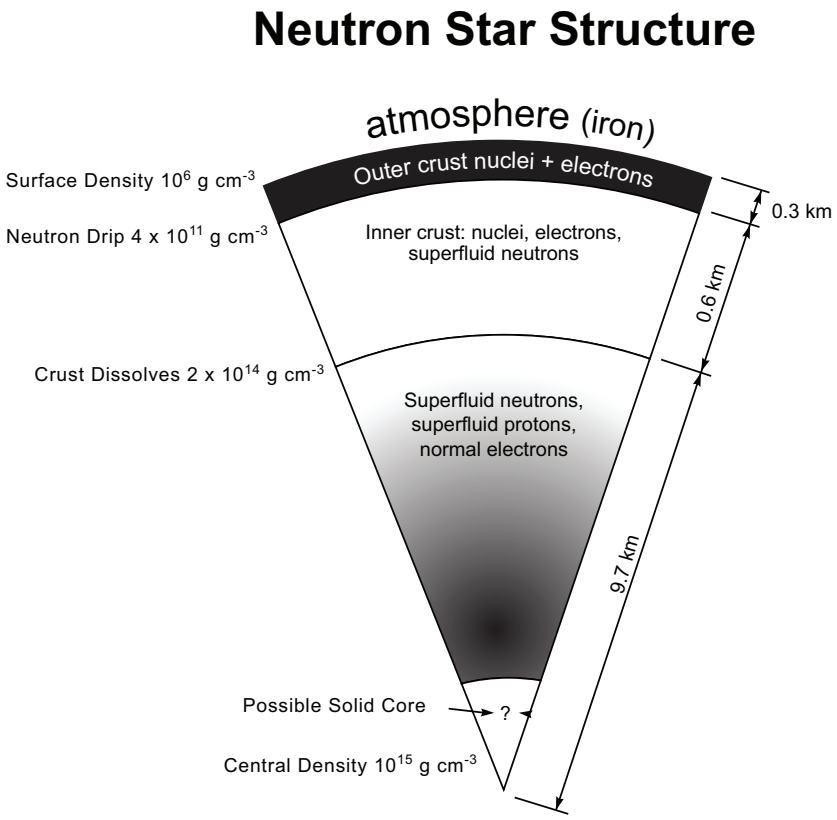

Figure 1. Neutron Star structure, reproduced from Shapiro & Teukolsky (1983).

a gas of relativistic electrons. Deeper in the crust, as the density increases the nuclei are increasingly neutron rich as it becomes energetically favorable for protons and electrons to combine to form neutrons via inverse beta decay.

At a density of $\sim 4 \times 10^{11}\,\mathrm{g\,cm^{-3}}$, a sea of neutrons begins to form around the lattice as neutrons "drip" from the nuclei. This neutron drip line distinguishes the outer crust from the inner crust. Several peculiar states of matter exist in the inner crust region. Within the inner crust free neutrons, by way of the attractive strong

nuclear force, are expected to form a neutron superfluid. As in liquid Helium (Migdal 1959), neutrons form up pairs of particles in two-body states, similar to Cooper pairs in the BCS theory. Pairs of neutrons, which are fermionic particles, behave like bosons. Below some critical temperature threshold, the neutron pairs condense into the lowest energy state, forming a viscosity-free fluid. This fluid moves through the coexisting nuclear lattice independently from the normal matter, allowing its rotation to be decoupled from the solid portions of the star. Additionally, nuclei begin to elongate to form exotic shapes near the crust-core boundary, the so called "pasta" phases (Ravenhall et al. 1983).

Approximately 1 kilometer below the surface, the density reaches that of nuclear matter, $\rho = 2.8 \times 10^{14}\,\mathrm{g\,cm^{-3}}$. It is at this point that the crust dissolves, while the neutron fluid remains along with a few percent protons by mass, and an equal number of electrons. The neutrons are predicted to be superfluid, and the protons are expected to be superconducting (Baym et al. 1971). For low mass neutron stars, this region extends inward to the center of the star. For larger stars, significant uncertainty remains as to the nature of the inner core. Because the equation of state of supernuclear matter is still uncertain, theoretical predictions of the central density and pressure cover a wide range. Various models of the neutron star equation of state predict that exotic states of matter, such as hyperons, meson condensates, and quark matter might constitute the inner core region (e.g., Sawyer & Scalapino 1973).

Though the surface represents a tiny fraction of a neutron star's mass, understanding the surface layers is key to understanding neutron star emission. For most neutron stars, outside the solid surface lies a thin atmospheric layer approximately 1 cm in thickness (Zavlin & Pavlov 2002). For stars with a low surface magnetic field, there may be an iron ocean above the solid lattice, outside of which is a partially ionized plasma atmosphere around 1 cm in depth. For highly magnetized or very hot stars, there is likely no atmosphere. In accreting stars, the picture is different, as there is an ocean full of impurities from accretion, and an accreted H/He atmosphere (Chamel & Haensel 2008).

Above the stellar surface strong magnetic fields create an electric field which strips charged particles from the surface, creating the magnetosphere, a plasma which is in corotation with the star (Goldreich & Julian 1969). This region is bounded by the light cylinder, defined by $\mathbf{\Omega} \cdot \mathbf{r} = c$. The radiation beam observed in radio pulsars originates near the surface, at a height of ~ 50 stellar radii for a pulsar with period $P = 1$s.

1.3. Plan of this Thesis

In this thesis, we will explore two topics related to the thermal and rotational dynamics of neutron stars. In chapter 2, we present details of timing irregularities observed in the spin rates of pulsars. In chapter 3, we will present evidence for time-correlated structure in pulsar timing noise. The correlations we observe may

be evidence of variable coupling between superfluid and solid components of neutron stars, similar to that observed in the post-glitch spin behavior of pulsars. In chapter 4, we summarize the thermal and magnetic evolution of neutron stars. In chapter 5, we show that a thermo-resistive instability may operate in the outer crusts of highly magnetized neutron stars. Such an instability leads to runaway heating of the crust, and may be related to flare activity in Soft Gamma Repeaters.

2. TIMING IRREGULARITIES IN PULSARS

Many important properties of neutron stars have been discovered through precision timing of their spin rates. This information comes from studies of pulse times of arrival (TOAs). Precision measurement of TOAs is a complex process: the pulse profile of each pulsar is unique, and varies from one pulse to the next (Figure 2). To accurately measure TOAs for a given pulsar, several minutes of pulses are recorded and subsequently folded at the assumed rotation period to arrive at a stable pulse profile which can be used for subsequent observations (Hobbs et al 2004). An accurate timing model for each pulsar is the product of many observing sessions, often spanning years. Several parameters are inferred from long term monitoring: the pulsar's rotational frequency and first derivative, position, proper motion, dispersion measure, and in the case of a binary system, orbital parameters and masses (Hobbs et al. 2004).

2.1. Glitches

All neutron stars observed to date have exhibited departures from deterministic spin-down. Two distinct types of irregularities have been observed: glitches and timing noise. Glitches are sudden increases in the star's spin frequency, often accompanied by a decrease in the spin-down rate (Figure 3). Glitch magnitudes from $10^{-10} \lesssim \Delta\Omega/\Omega \lesssim 10^{-6}$ have been observed. Though over 300 glitches have been detected do date (Espinoza et al. 2011), many pulsars have exhibited only a single

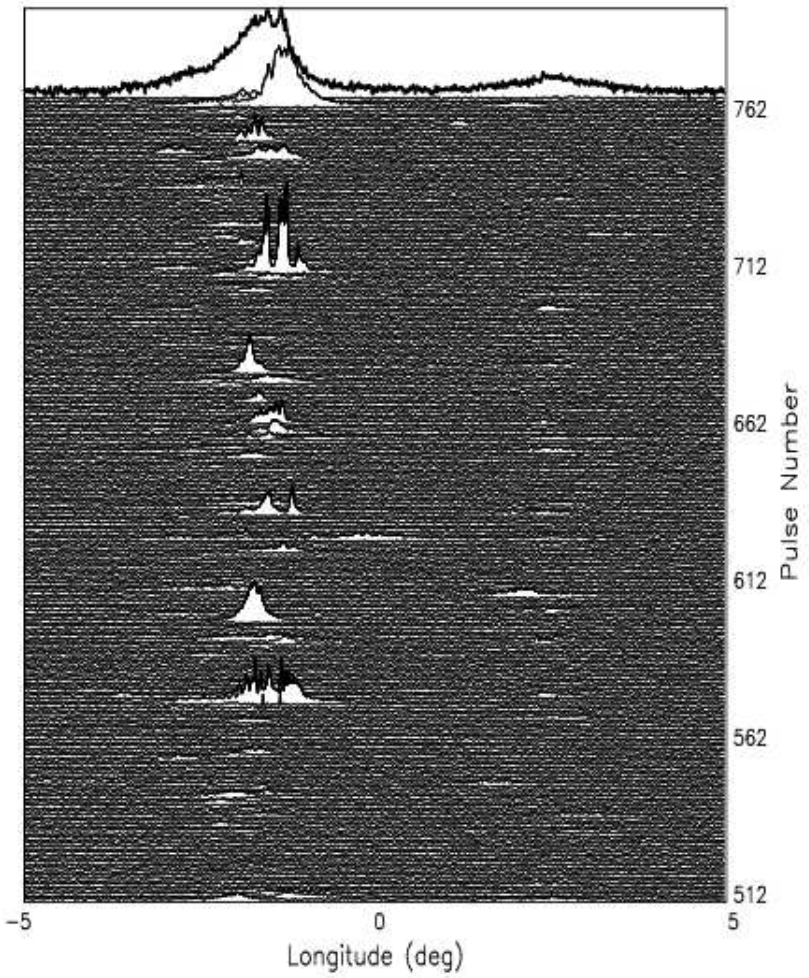

Figure 2. Several hundred individual pulses from PSR B1133+16. The thick line at the top represents the integrated profile for the observing session. From Honnappa et al. (2011).

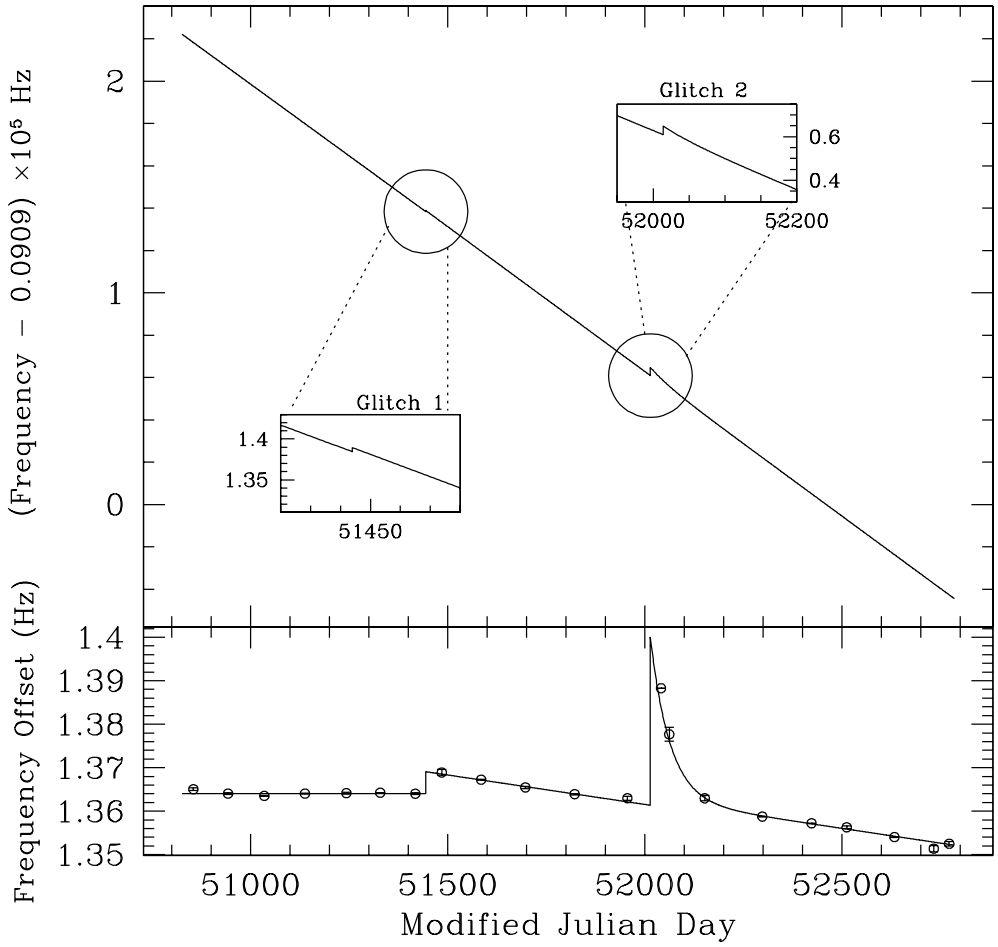

Figure 3. Glitches observed in magnetar 1RXS J1708-4009 (Kaspi et al. 2003).

glitch. For the more active objects, waiting times between glitches range from months to years. The spin-up occurs very quickly - a glitch in the Vela pulsar was unresolved even though pulse arrival times were sampled every minute (Dodson et al. 2002). Immediately after a glitch, relaxation of the spin rate is often observed, characterized by decay over timescales from days to years (Table 1, and Figure 3). The healing parameter Q, the fraction of the glitch magnitude which is eventually recovered after

Name	Epoch (MJD)	$\Delta\nu/\dot{\nu}(10^{-9})$	τ (d)	Q	Ref
J1048-5832	49034	2995	100	.025	d
J1048-5832	50788	771	400	.245	d
J1341-6220	48645	990	75	.02	d
J1341-6220	50008	1636	300	.004	d
J1709-4428	48778	2012	1420	.133	d
J1731-4744	49387	135	263	.079	d
J1731-4744	50703	2.6	250	.25	d
J0835-4510	40280	2340	-	.030	a
J0835-4510	42683	1990	-	.088	a
J0835-4510	43693	3060	-	.024	a
J0835-4510	44888	1145	-	.183	a
J0534+2200	40493	4	5	.94	a
J0534+2200	41250	2	15.2	.96	b
J0534+2200	41163	2.2	5.7	.92	c
J0534+2200	42448	44	15.5	.70	a
J0534+2200	43023	1.1	8	.70	c
J0534+2200	43768	2.8	8	.70	c
J0534+2200	46664	4.1	9.3	.10	a
J0534+2200	47768	85	18	.89	a

Table 1. Glitch characteristics of selected pulsars. References: [a] (Lyne et al. 2000), [b] (Lohsen 1975), [c] (Lohsen 1981), [d] (Wang et al. 2000).

the glitch varies widely from one pulsar to another. Some objects, such as the Crab pulsar often show almost complete recovery, while others like the Vela pulsar recover only a fraction of the glitch spin-up.

Early glitch models attributed the unusual spin behavior to starquakes (Ruderman 1969), which produce an abrupt change to the star's moment of inertia. As the star spins down under the influence of electromagnetic torque, stress builds on the solid crust leading to eventual fracture. The decrease in moment of inertia leads to an increase in rotation rate, as angular momentum is conserved. However, pulsars

exhibit glitches too frequent and large in amplitude to be caused by starquakes, and the starquake model is not viable.

More recent models attribute glitch activity to the transfer of angular momentum from the superfluid components of the star to the crust (Anderson & Itoh 1975, Link et al. 1993, Larson & Link 2002). In this model, the fluid interior spins faster than the crust, acting as an angular momentum reservoir which is episodically tapped to spin up the crust. Angular momentum transfer may be triggered by starquakes, or the sudden unpinning of superfluid vortices, as we now explain.

The bulk superfluid must be irrotational; the rotating fluid has an array of quantized vortices, or microscopic filaments of normal matter around which the superfluid circulation will be non-zero. The macroscopic velocity field of the superfluid is then determined by the number and spatial distribution of the vortices. When free to move throughout the superfluid, vortices will form an arrangement which brings the fluid into co-rotation with the normal matter. However, in some regions of the star an attractive force exists between the vortices and normal nuclei which may fix them in place (Donati & Pizzochero 2003, Avogadro et al. 2008). As the crust spins down due to magnetic braking, the velocity lag between vortices and the superfluid creates an outward directed lift force, or Magnus force. If the pinning force is greater than the Magnus force on the vortices, the fluid component will maintain a constant angular velocity and differential rotation will develop between the crust and liquid. In the event of catastrophic unpinning, the angular momentum stored in the vortex lattice

may be transferred to the crust, resulting in a glitch (Anderson & Itoh 1975, Alpar et al. 1984, Link et al. (1993), Larson & Link 2002) . Many of the observed properties of glitches are well fit by the glitch models of Alpar et al. (1984), Link et al. (1993), and Larson & Link (2002).

2.2. Timing Noise

Though not all pulsars have exhibited glitches, all pulsars observed to date exhibit variations in their pulse times of arrival with respect to predicted arrival times. These variations, *timing noise*, often appear to take the form of quasi-periodic wander (Figure 4).

Early study of the statistics of timing noise in pulsars was performed by Boynton et al (1972) using two years of observations of the Crab pulsar. After attempting to fit a timing model to the observations, the authors determined that no simple function could fit the observed timing variations. Later efforts attempted to classify timing noise as a random walk in either the rotational phase, frequency, or frequency derivative (Cordes, Helfand 1980). Further studies determined that the strength of timing noise is correlated with the rotation period derivative (Arzoumanian et al. 1994). Hobbs et al. (2010) have produced the most extensive timing noise study to date, analyzing 366 pulsars covering 36 years of data. They conclude that the complexity of timing noise cannot be explained by high frequency random walks in the pulsar spin parameters, as had been assumed in the past.

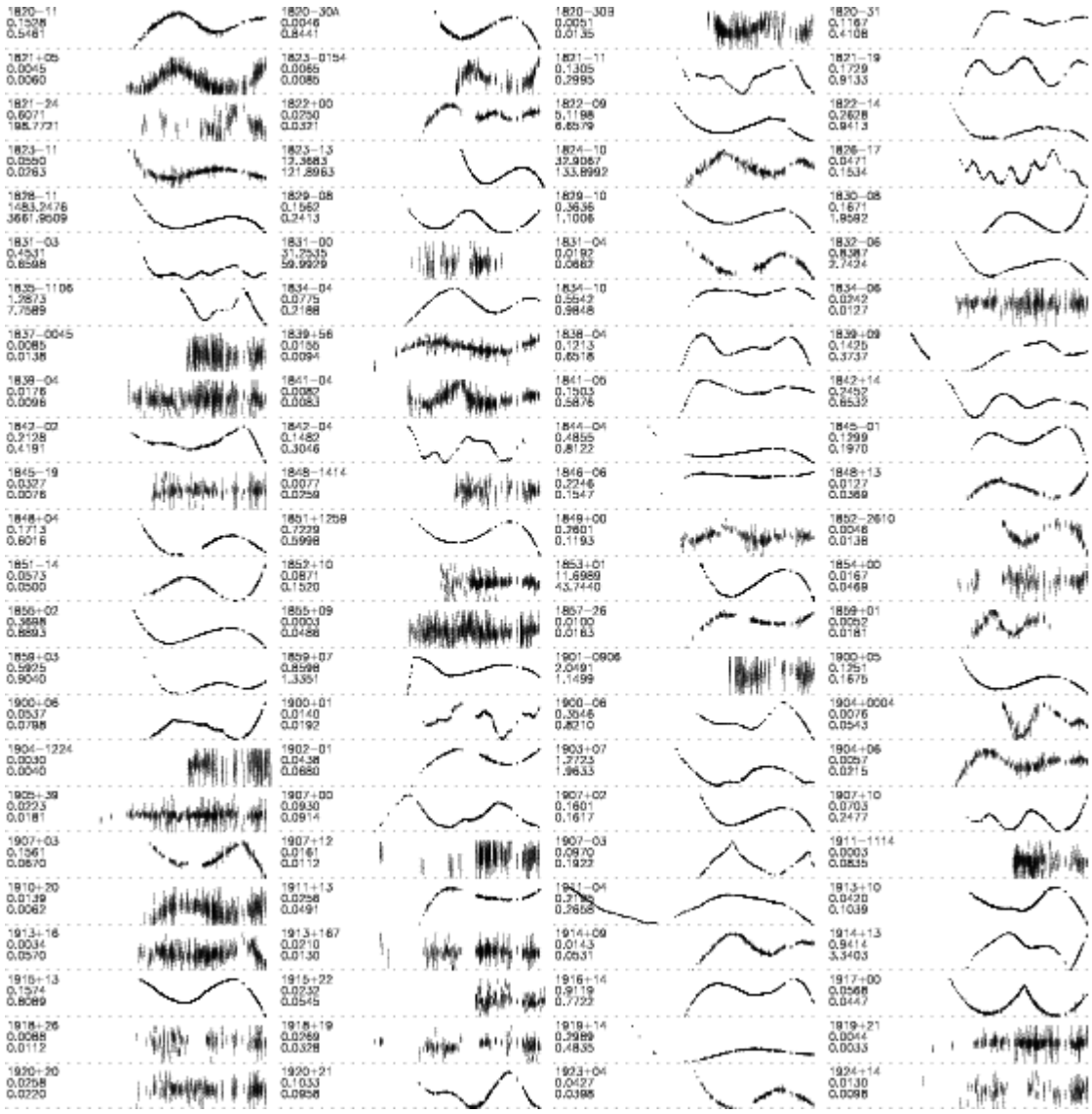

Figure 4. Representative sample of timing residuals, from Hobbs et al. (2010).

The timing noise process is very complex. The source of timing noise is still not understood, and may reside originate inside the neutron star, outside, or both. Possible sources within the star include precession of the neutron star crust (Link & Epstein 2001) , variable coupling between the fluid and crust components (Alpar et al. 1986), and changes in the star's shape (Cordes 1993). Additionally, small amplitude glitch-like events may contribute to timing noise. Hobbs et al. (2010) find that recovery from past glitches may explain many features of timing noise in young ($\tau_c < 10^5$ yr) pulsars.

Variations in the external electromagnetic spin-down torque on the star may also contribute (Cheng 1987a, Cheng 1987b, Urama et al. 2006), associated with dynamics in the magnetosphere. Lyne et al. (2010) find that for several pulsars, timing noise is correlated with changes in the pulse shape. Since the pulsed radio emission originates several hundred kilometers above the surface of the star, they conclude that changes in the pulsar magnetosphere may be responsible for timing noise. Accretion of matter onto the stellar surface, and the effects of asteroids on the magnetosphere may also play a role in timing noise (Cordes & Shannon 2008) .

While theories on the source of timing noise abound, several possible sources of timing noise have been ruled out (Hobbs et al. 2010). Coincident observations of pulsars from multiple sites, using several different timing analysis methods, indicate that timing noise does not originate from observing hardware or data processing. Timing observations at multiple frequencies reveal that changes in interstellar dispersion are

not responsible for long term features. This result is confirmed by evidence that timing noise is not correlated with height above the galactic plane. Pulse shape changes are also not a likely source of timing noise, as timing residuals are often much larger than the pulse width.

Timing noise is therefore thought to represent variations in the spin rate of the neutron star. A more complete understanding of timing irregularities in pulsars may give insight into neutron star evolution and the structure of their interiors. In Chapter 3, we present evidence of time-correlated structure in pulsar timing noise. We interpret these correlations as the signature of a relaxation timescale between the crust and fluid components of the star.

3. TIME CORRELATED STRUCTURE IN PULSAR TIMING NOISE

In this chapter, we explore several methods that can be used to look for structure in pulsar timing noise. We show that analysis methods in the time domain are best suited for revealing structure in noisy time series, as is typically the case for pulsar data. We develop two methods of analysis, the *discrete correlation function* and the *lagged dispersion function*, and analyze timing data of 32 pulsars. These methods reveal clear correlations over a timescale $\tau = 10 - 40$ d in timing noise for two pulsars: PSR B1133+16 and B1933+16. We interpret the correlation as the signature of a relaxation mode of the star, indicating a coupling timescale between the fluid and crust components. Material in this chapter is in preparation for publication.

3.1. Introduction

The response of a complex system to stochastic perturbations can reveal much about the dynamical properties of the system. In this connection, a complete characterization of the stochastic spin variations seen in isolated neutron stars has been of considerable interest since the discovery of pulsars in 1967. As described in Section 2.2, timing noise is likely due to many contributing processes, each acting on the neutron star crust to produce a complex response of the spin rate. From the standpoint of doing neutron star seismology, the complexity of timing noise is an advantage; regardless of its origin, timing noise will excite at some amplitude all of the rotational modes of the system, such as, damped differential rotation, rotational modes in the

superfluid interior (such as Tkachenko modes), precession (nutation) and resonances such as crust shear modes. Hence, the presence of any structure in the noise that has a timescale would serve as a probe of the dynamics of the combined system of solid crust and liquid interior. As a simple analogy, in an RC circuit driven by thermal fluctuations, the time constant can be determined by constructing a time series of the current through the resistor as a function of time. Though the circuit never relaxes to equilibrium, the relaxation mode is excited by the noise in the circuit, allowing measurement of the RC constant.

The coupling between the crust and core probably occurs through a combination of magnetic stresses and dissipative torques associated with the motion of quantized vortices, giving a complicated spectrum of damped modes and possibly resonances. Resonances might be detectable as peaks in the power spectrum of fluctuations, broadened by damping processes. For a system with a purely damped differential rotation mode, associated with, for example, friction between the crust and a portion of the liquid interior, stochastic perturbations from rotational equilibrium by the noise process would never relax completely. In this case, decoupling by fluctuations at frequencies higher than the damping frequency τ_d^{-1} would increase the spectral power for all frequencies above τ_d^{-1} by a magnitude determined by the ratio of moments of inertia of the crust and the liquid to which it is imperfectly coupled (Lamb et al. 1978). Past studies of timing noise power spectra have not, however, revealed structure beyond the power-law that is the hallmark of a noisy process. That is, no deviations from

rigid-body rotation have yet been revealed (Boynton & Deeter 1979, Boynton 1981, Boynton et al. 1984). The only evidence to date that neutron stars do not rotate rigidly comes from glitches, whose occurrence and subsequent recovery have been attributed to variable coupling between the crust and the liquid interior (Alpar et al. 2004, Link et al 1993, Pizzochero 2011, see Section 2.1). Why neutron stars have not shown evidence for deviations from rigid body rotation as they are constantly perturbed by timing noise has been an important unanswered question in neutron star physics for over three decades.

Here we report the first evidence for temporal correlations in pulsar spin fluctuations. We find that excursions of the phase from the mean are correlated over a timescale of $\sim 10 - 40$ d in two pulsars. Over timescales less than this correlation time, the size of a phase excursion is correlated with previous excursions; over longer time scales the phase excursions become decorrelated.

3.2. Analysis Methods

3.2.1. High Pass Filtering

Timing noise typically appears as wander on timescales of months to years, as shown in Figure 5 for PSR B1818-13. The relaxation timescales of pulsars during post-glitch recovery range from days to months. To best search for similar timescales in timing noise data, we found it necessary to "whiten" these data by applying a high pass filter.

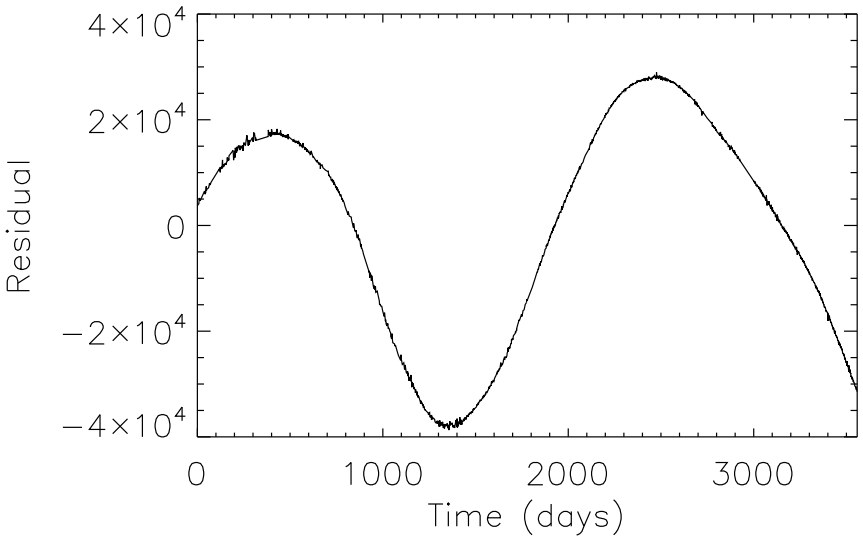

Figure 5. Timing Residuals for PSR B1818-13. Long period wander evident in the object is typical for timing noise in the pulsars we study.

To illustrate the whitening method, we construct simulated timing residuals $\delta t(t)$ consisting of periodic functions, quasi-periodic wander and gaussian noise,

$$\delta t(t) = \sum_i \left(\frac{A_i}{\omega_i} sin(\omega_i t + \phi_i) \right) + P(t) + N(t), \tag{3.1}$$

where A_i, ω_i, and ϕ_i are the amplitude, frequency, and phase of the sine waves, respectively, $P(t)$ is an arbitrary polynomial function, and $N(t)$ is gaussian noise. A_i and ϕ_i are randomly generated values. The sine waves are weighted by the frequency ω_i to produce a red power spectrum, similar to that of typical pulsar data. An example of a simulated time series is shown in Figure 6, using a sum of 10 sine waves. In this example, the frequencies ω_i are harmonically related, with a maximum frequency $\omega_1 = 0.32$, and minimum frequency $\omega_{10} = 6.25 \times 10^{-4}$.

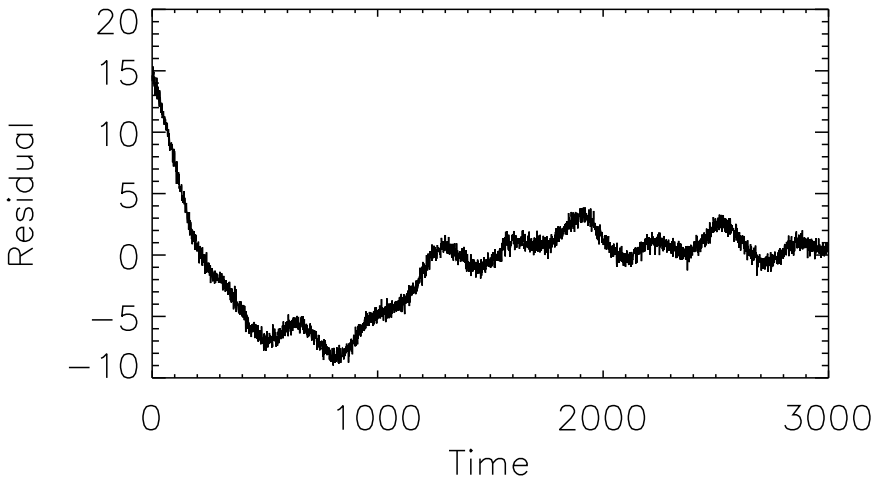

Figure 6. Simulated timing residuals consisting of 10 sine waves, an arbitrary 5th order polynomial, and Gaussian noise.

We divide the time series into blocks of width W and calculate the average value of the residuals in each block. Using unweighted least squares fitting, we use a cubic spline function to smoothly fit the average residual values for each block. Blocks are contiguous but non-overlapping so as to not introduce correlations. We then calculate the values of the fitting function at the original time series sampling times by interpolation. The fitting function is then subtracted from the original time series to produce whitened residuals. Several examples of fitting functions are shown in Figure 7 for the simulated time series shown in Figure 6.

The effect of whitening for different values of the filter width W can be seen by calculating the autocorrelation function of the whitened residuals. The autocorrelation function measures the similarity of a time series to itself upon translation in time

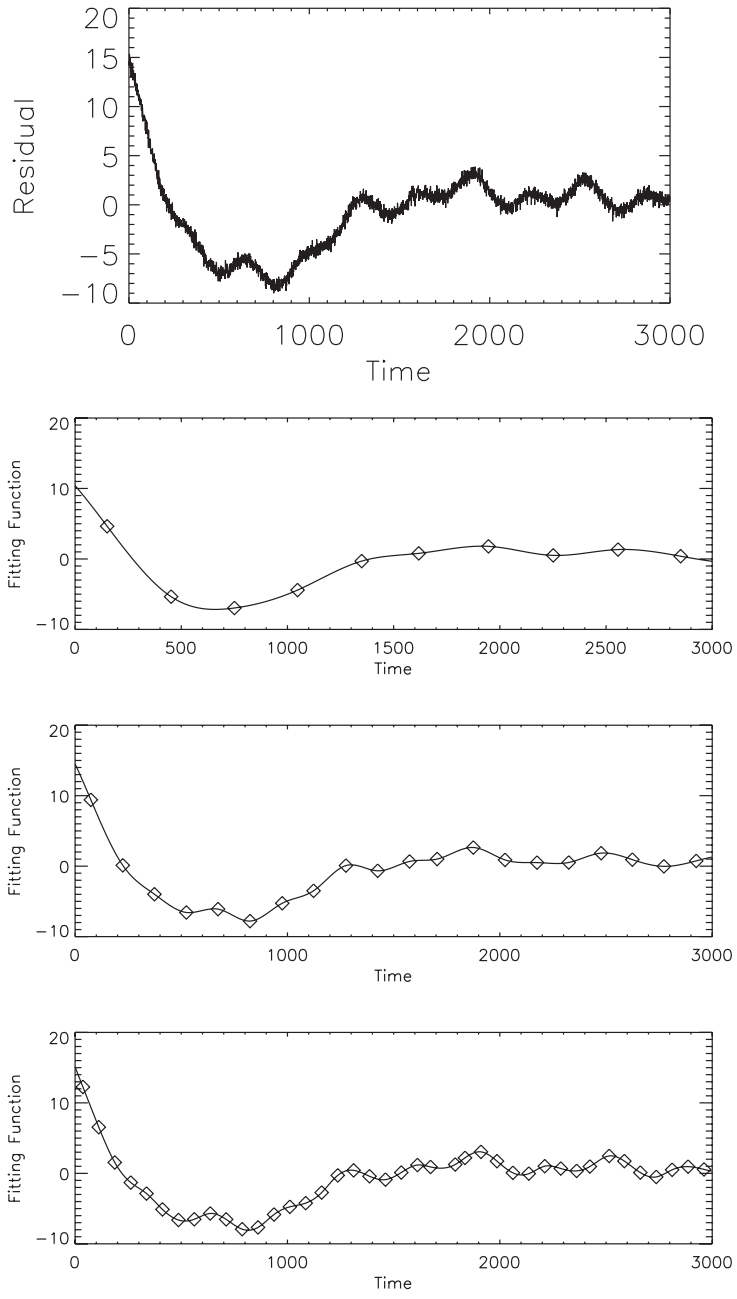

Figure 7. Examples of fitting functions used to whiten the simulated timing residuals. Top panel - simulated timing residuals. 2nd panel - fitting function using $W = 300$. 3rd panel - fitting function using $W = 150$. Bottom panel - fitting function using $W = 75$. Diamonds represent the average values of the residuals in each data block of width W used for the cubic spline fitting.

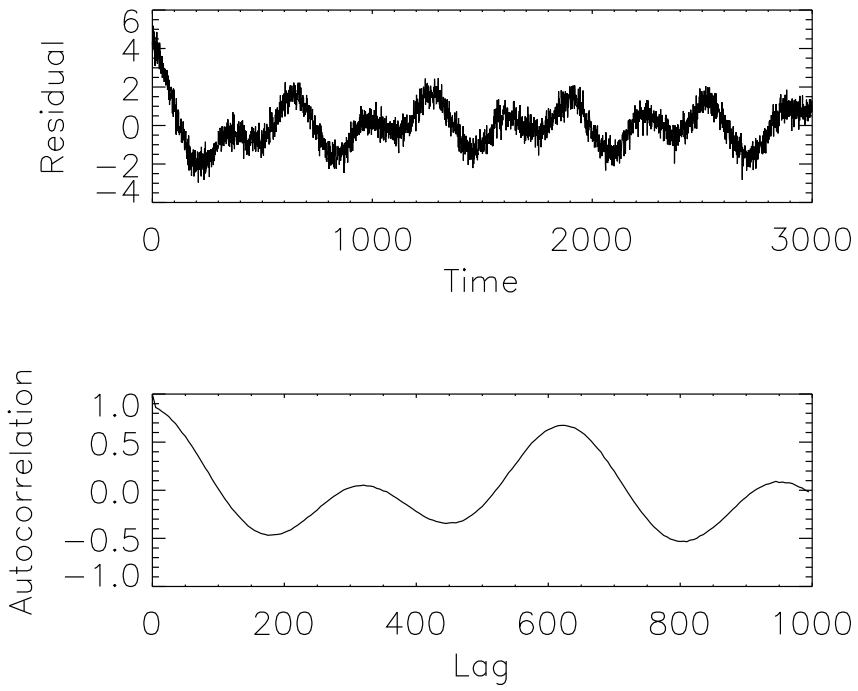

Figure 8. Top panel - Timing residuals after whitening for $W = 300$. Bottom panel - Autocorrelation function of the time series. Significant long period wander is still evident.

by a given lag τ,

$$ACF(\tau) = \sum_t \frac{(X_t - \mu)(X_{t+\tau} - \mu)}{\sigma^2}, \tag{3.2}$$

where X_t is the value of the time series at time t, μ is the mean of X_t, and σ is the square root of the variance of X_t. In this example, for $W = 300$ the polynomial has been removed well, but significant periodicity remains in the time series (Figure 8). For $W = 150$, some of the periodicity has been removed, but high frequency components are still apparent (Figure 9). Using a filtering parameter $W = 75$ removes all

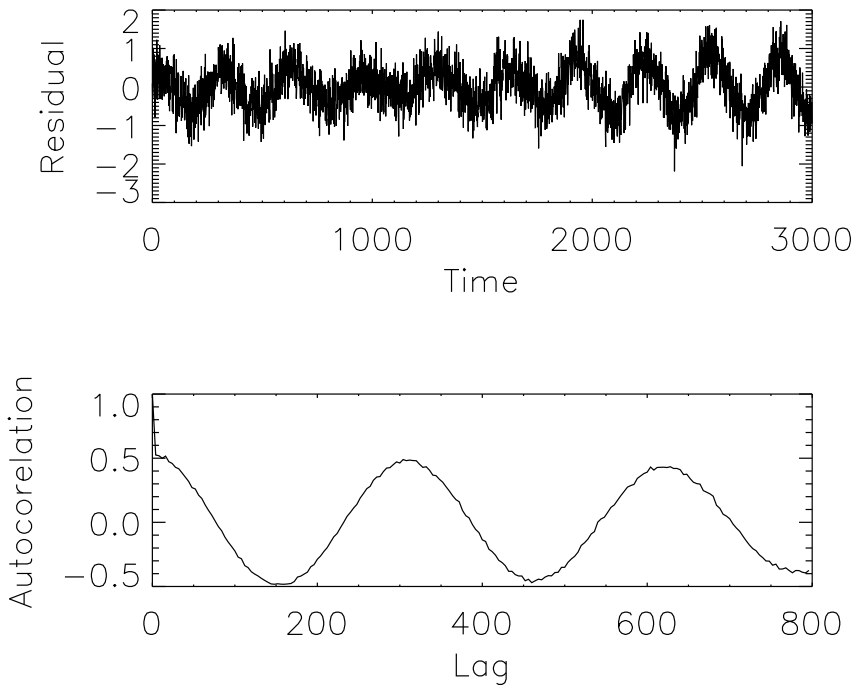

Figure 9. Top panel - Timing residuals after whitening for $W = 150$. Bottom panel - Autocorrelation function of the time series. Periodicity remains in the time series.

the wander in the time series, leaving a correlation function consistent with Gaussian noise (Figure 10).

Anti-correlations arise if our choice of W is too small. When W becomes comparable to the characteristic time over which the whitened time series changes sign, the fitting function begins to fit the noise. This results in a whitened time series which is anti-correlated for lags $\tau < W$ (Figure 11), as fitting the noise produces residuals which are more likely to be of opposite sign. To see this, consider the limiting case in which each box of width W contains only two points. The average value of each box is subtracted from the time series, resulting in data that are perfectly anti-correlated

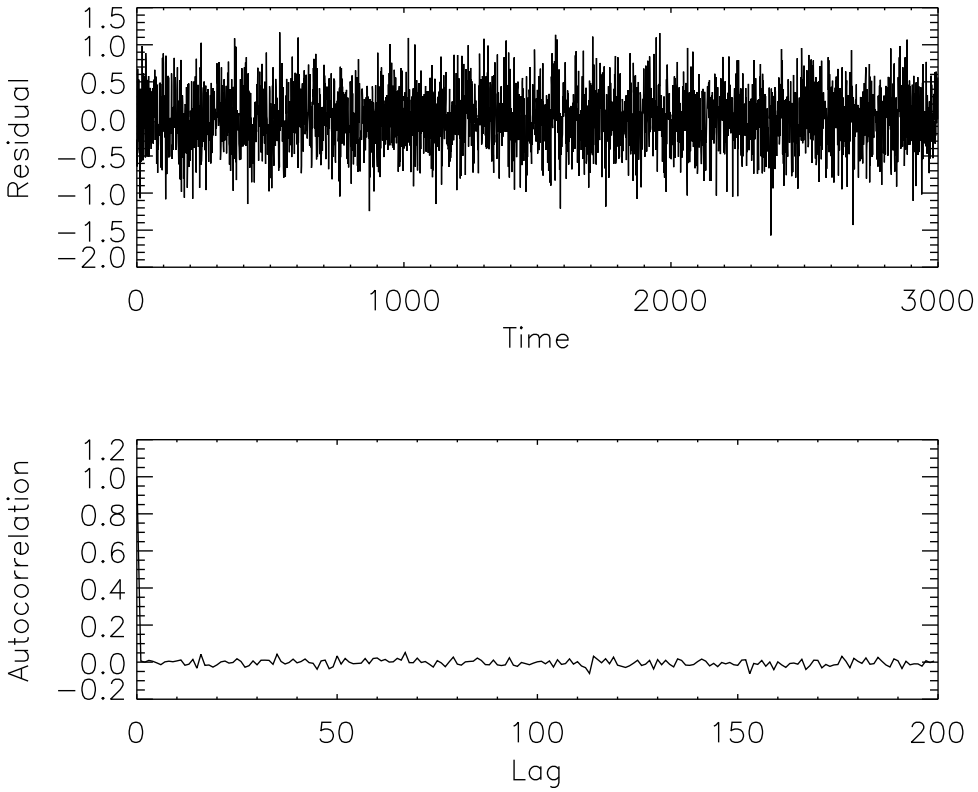

Figure 10. Top panel - Timing residuals after whitening for $W = 75$. Bottom panel - Autocorrelation function of the time series. All wander and periodicity has been removed by the whitening process, leaving a correlation function consistent with noise.

for a lag $\tau = 1$. In general, the anti-correlation due to overwhitening is strongest for a lag $\tau \simeq W/2$. This distinct signature allows us to easily determine if the filtering parameter we use is too small.

3.2.2. Time Domain Techniques

Power spectrum analysis is often poorly-suited for the analysis of noisy data (or signal with noise-like properties); the FT of rapidly-varying data spreads the power over a large range of frequencies, producing a power law or white noise spectrum from

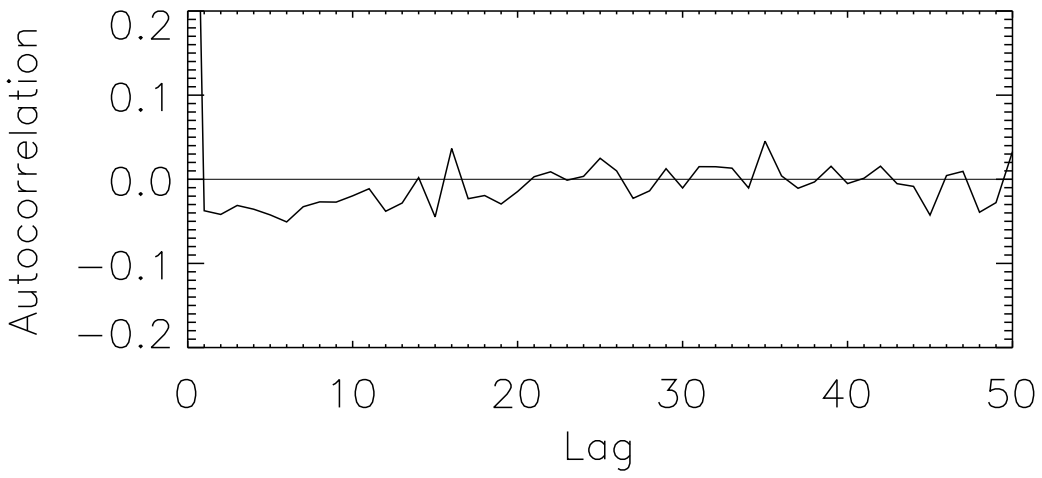

Figure 11. Autocorrelation function of the time series in Figure 6, after whitening with $W = 20$, revealing anti-correlation at low lag, the signature of overwhitening. The anti-correlation is strongest for lags $\sim W/2$.

which it can be difficult or impossible to identify structure with any confidence. (The complex FT does not destroy data, of course; in principle correlations not seen in the power spectrum could be detected from the phase information contained in the FT). For example, Fourier analysis of timing noise in PSR B1933+16 reveals only red noise (Figures 12).

To illustrate the effectiveness of time domain versus frequency domain analysis, we consider an example based on a simple physical model for a neutron star with an internal degree of freedom. The interaction between the fluid component and crust component of the star is described by

$$I_c\dot{\Omega}_c = N_{ext} - \frac{I_c(\Omega_f - \Omega_c)}{\tau_c}, \tag{3.3}$$

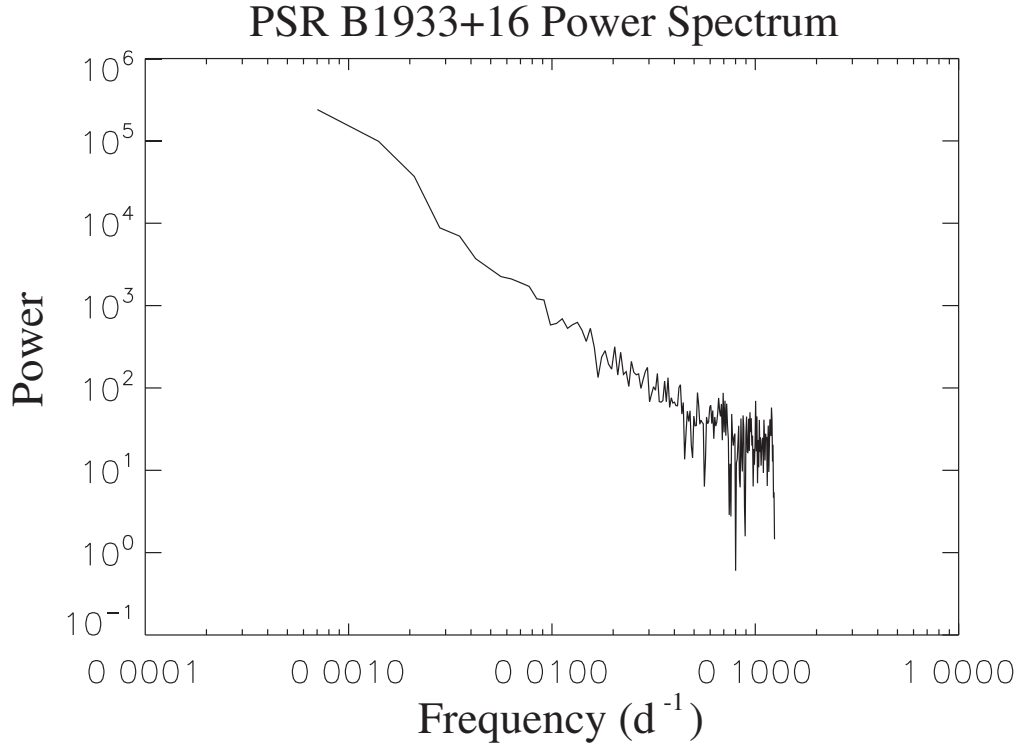

Figure 12. Power spectrum for PSR B1933+16.

$$I_f \dot{\Omega}_f = \frac{I_c(\Omega_f - \Omega_c)}{\tau_c}, \tag{3.4}$$

where I_c and I_f are the moments of inertia for the crust and fluid, respectively, Ω_c and Ω_f are the rotation rates of the crust and fluid, τ_c is the coupling timescale between the crust and fluid, and N_{ext} is the external torque on the crust. Combining Eqs. (3.3) and (3.4) to eliminate Ω_f gives the differential equation for the crust component,

$$\ddot{\Omega}_c + \frac{1 + I_c/I_f}{\tau_c}\dot{\Omega}_c = \frac{\dot{N}(t)}{I_c} + \frac{N(t)}{I_f \tau_c}. \tag{3.5}$$

To construct a simple model of neutron star spin behavior, we consider crust and fluid components initially in co-rotation, with a ratio of moments of inertial $I_c/I_f = 1$

for illustration. We perturb the crust with a series of δ-functions,

$$N(t) = \sum_i A_i \delta(t), \tag{3.6}$$

where A_i are randomly generated amplitudes. This model for the external torque represents a series of instantaneous transfers of angular momentum to the crust, regardless of the exterior source or sources. In between impulses, the crust rotation rate can be solved exactly,

$$\Omega_c(t) = \Omega_1 \frac{I_f}{I_{tot}} e^{-t/\tau} + \Omega_2, \tag{3.7}$$

where Ω_1 and Ω_2 are constants depending on initial conditions, $I_{tot} = I_f + I_c$, and $\tau = (I_f/I_c)\tau_c$. Using this model, we construct a time series of frequency residuals shown in Figure 13.

The frequency response of the crust to the external torque N_{ext} is found by Fourier transforming Eq. (3.5), giving

$$|\Omega_c(\omega)|^2 = \frac{1}{\omega^2 \tau_c^2} \left[\frac{(\omega\tau_c)^2 + (I_c/I_f)^2}{(\omega\tau_c)^2 + (I/I_f)^2} \right] |N_{ext}(\omega)|^2 \tag{3.8}$$

At frequencies higher than $\omega\tau = 1$, only the crust responds to the external torque. At lower frequencies, the entire moment of inertia of the star I_{tot} is perturbed by the torque, resulting in a lower response. We define the response function as the frequency dependent term in brackets, shown in Figure 14. This term gives in a "knee" in the spectrum around $\omega\tau = 1$. Such a knee is evident in the power spectrum of the simulated phase residuals (Figure 13 - bottom panel).

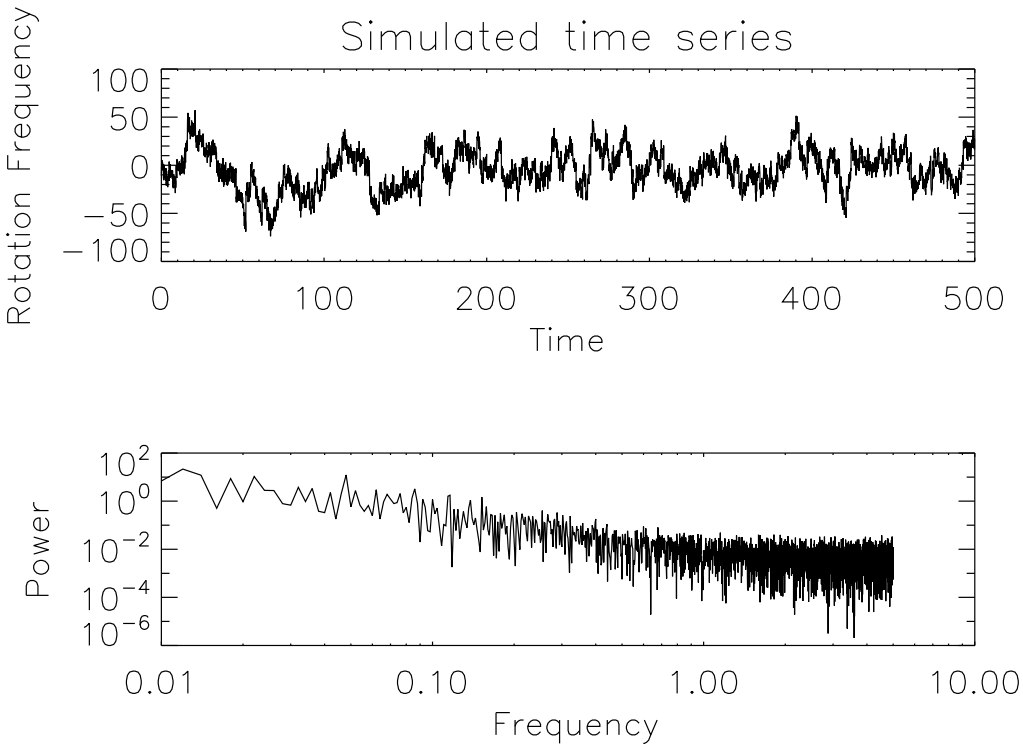

Figure 13. Top panel - Simulated frequency residuals with data correlated over a timescale $\tau = 1$. Bottom panel - The power spectrum of the frequency residuals, indicating a "knee" at $\omega\tau \sim 1$.

In Figure 15, we have added gaussian noise to the time series to simulate noisy data. In this case, the knee in the spectrum revealing the coupling timescale τ_c becomes buried beneath the noise. Time domain analysis is better suited for this noise-dominated time series. We calculate the autocorrelation function of the time series shown in Figure 15 for various lags. The autocorrelation function (Figure 16) is still easily able to identify the coupling timescale buried beneath the noise.

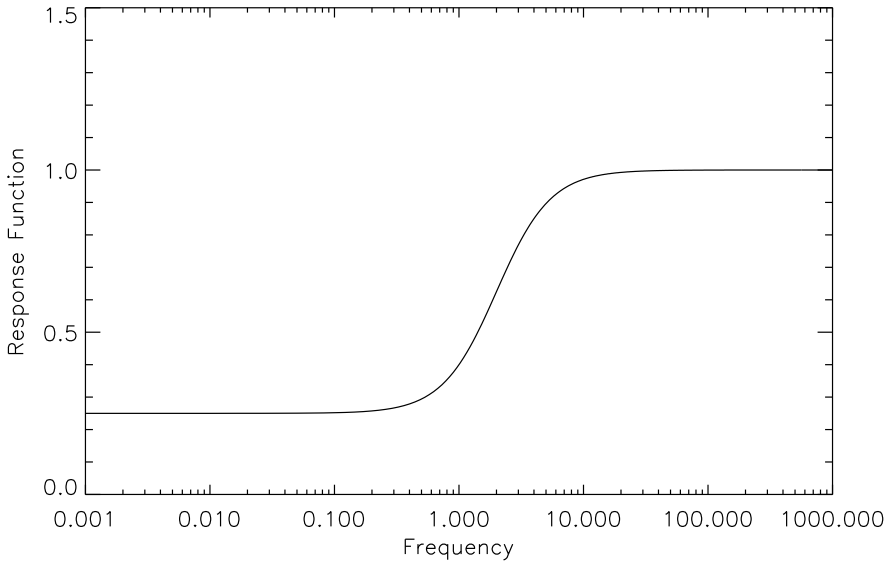

Figure 14. Frequency dependent response function of the crust to external torque. The knee in the center of the plot represents the transition from coupled to uncoupled components of the star as the star is perturbed at various frequencies.

Discrete Correlation Function. Time domain techniques maximize our ability to identify subtle correlations, as shown in the previous section. Our pulsar timing data are unevenly sampled, however, the typical situation for astronomical data. It is desirable to measure autocorrelations without having to bin the data, which would restrict our analysis to a timescale no shorter than the longest gap in the data and entail a severe loss in time resolution. Unevenly-sampled data is readily handled with the discrete correlation function $DCF(\tau)$ (Edelson & Krolik 1988). For a set of arrival time residuals δt_i this quantity is calculated as follows. We first construct the matrix

$$DCF_{ij} = \frac{(\delta t_i - \overline{\delta t})(\delta t_j - \overline{\delta t})}{\sigma^2}, \tag{3.9}$$

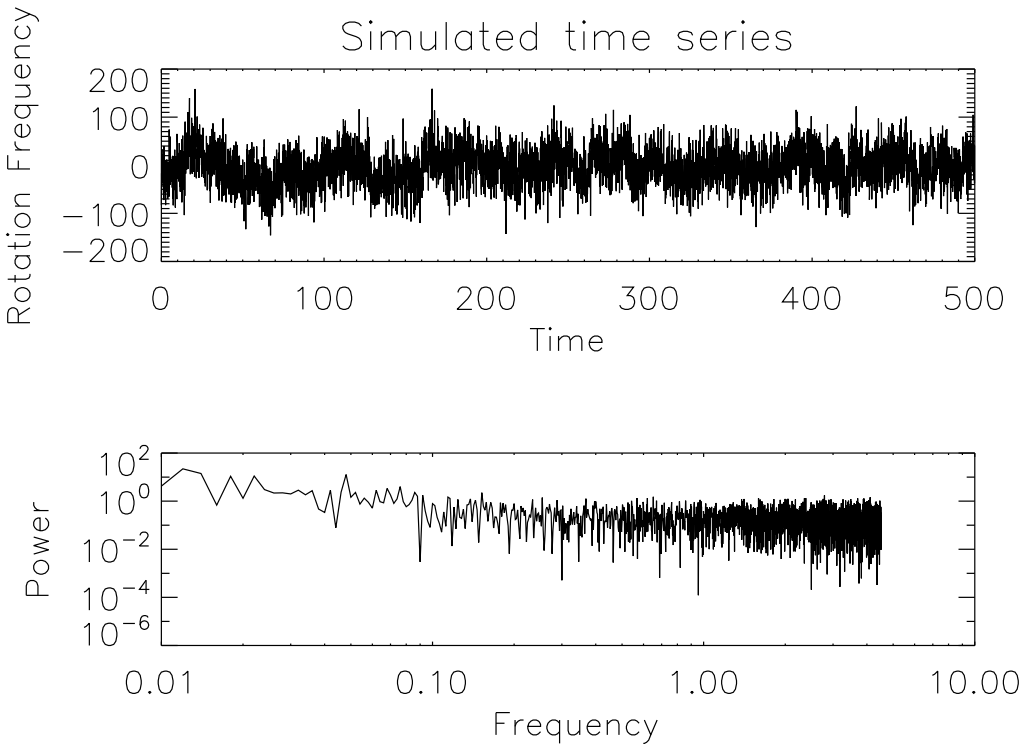

Figure 15. Top panel - Identical frequency residuals to Figure 13, but with Gaussian noise added to each data point. Bottom panel - The power spectrum of the frequency residuals. After the addition of noise to the time series, the coupling timescale is no longer evident.

where $\overline{\delta t}$ is the mean of the data set and σ is its standard deviation (the choice of normalization is arbitrary). This matrix is calculated for all possible pairs $(\delta t_i, \delta t_j)$, each of which is associated with a pairwise lag $\Delta t_{ij} \equiv t_j - t_i$. Suppose that there are M pairs that satisfy the condition

$$\tau - \Delta\tau/2 \leq \Delta t_{ij} < \tau + \Delta\tau/2, \tag{3.10}$$

where $\Delta\tau$ is the width of the sampling window. Averaging over the M pairs that satisfy Eq. (3.10), gives

$$DCF(\tau) = \frac{1}{M} \sum DCF_{ij}. \tag{3.11}$$

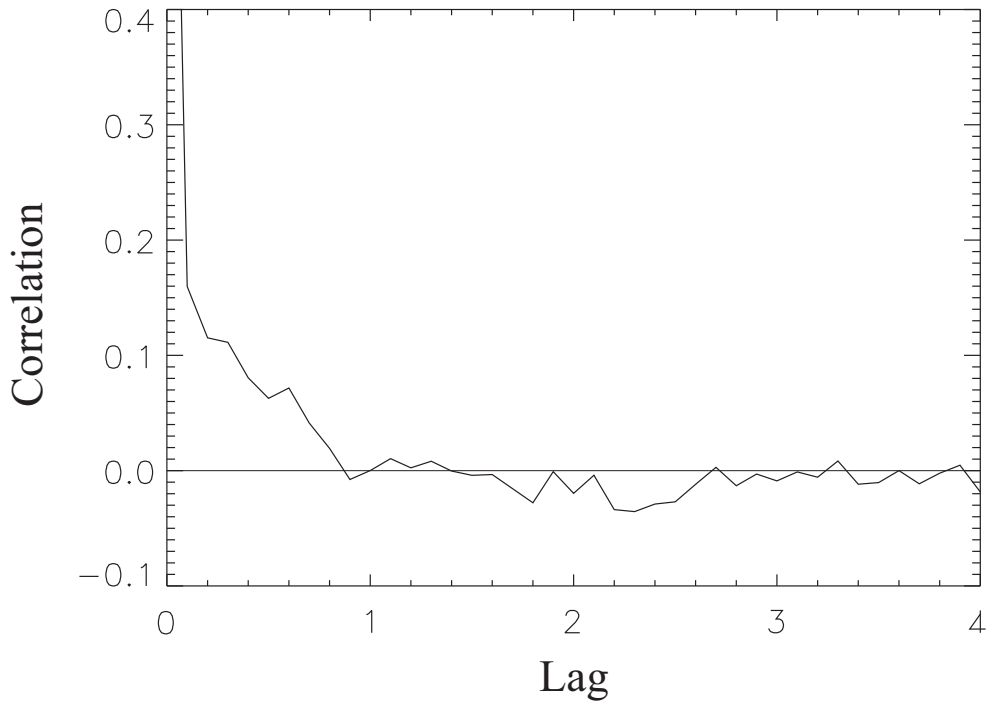

Figure 16. The autocorrelation function for the time series shown in Figure 15 (top panel), revealing the intrinsic relaxation time of the system that is not visible in the power spectrum.

Points that do not fall in the sampling window do not contribute to $DCF(\tau)$. The window size is minimized so as to maximize resolution without loss of good statistics; in practice, $\Delta\tau$ can be taken to be almost as small as the average sampling time. This procedure uses every data point, without any significant penalty in resolution due to occasional large gaps in the data. The values of τ that are used are binned in units of $\Delta\tau$, but the data remain unbinned. The standard uncertainty in the $DCF(\tau)$ is (Edelson & Krolik 1988)

$$\sigma_{\rm DCF}(\tau) = \frac{1}{M-1}\left\{\sum \left[DCF_{ij} - DCF(\tau)\right]^2\right\}^{1/2}. \qquad (3.12)$$

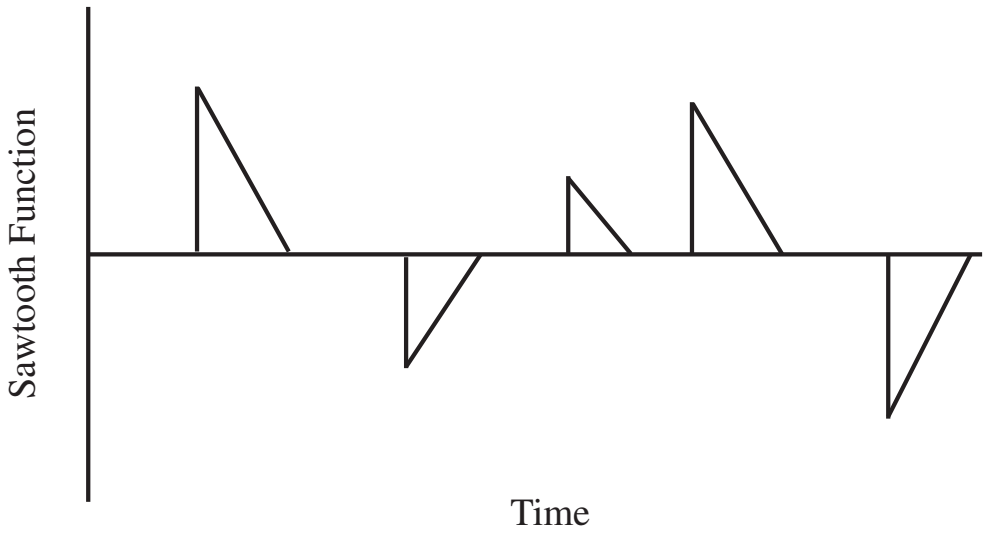

Figure 17. Schematic of the sawtooth function. Each impulse decays linearly over a timescale of 10 units. Impulses are randomly spaced in time, with random amplitudes of either sign drawn from a Gaussian distribution with a standard deviation of unity.

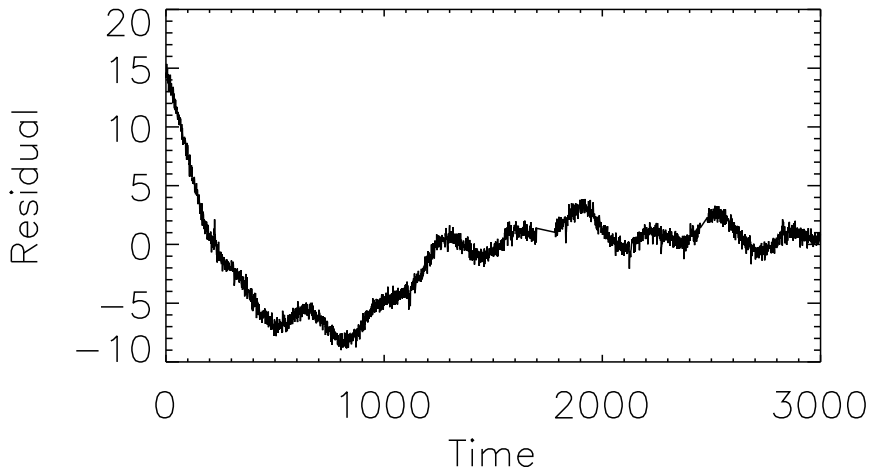

Figure 18. Simulated residuals consisting of periodic functions, a polynomial, Gaussian noise, and a sawtooth function. Several gaps are added to simulate real data. The sawtooth function, with average amplitude ±1, is too small to be seen by eye.

To illustrate that the DCF can distinguish between correlations due to wander and those due to a relaxation process, we add a series of 10 "sawtooth" functions to the simulated time series shown in Figure 6. Each sawtooth consists of a discontinuous jump of random magnitude, followed by a linear decay over 10 time units. The jumps are randomly spaced over the time series, with magnitudes drawn from a Gaussian with a standard deviation of unity, such that the jumps of average magnitude ± 1 are undetectable to the eye (Figure 18). An illustrative representation of the sawtooth function we use is shown in Figure 18. We have also added gaps to simulate real data.

Upon removal of the red noise, several DCFs for this time series are shown in Figure 19. For $W = 75$, only positive correlations over ~ 10 time units are found (top panel), as the low-frequency wander has been almost completely subtracted. This DCF signature is easily differentiated from that of short timescale wander, which contains both correlations and anti-correlations. At lower values of W, the fitting function begins to remove correlations in the data (middle and bottom panels); the data have been overwhitened. For a broad range in W, we can see the correlations.s

We conclude that high-pass filtering of the time series followed by calculation of the DCF is a robust method for identifying an intrinsic relaxation timescale t_{corr}, provided the following condition is satisfied:

$$t_{samp} < t_{corr} < t_{wander}, \tag{3.13}$$

where t_{samp} is the mean sampling interval and t_{wander} is the shortest timescale of the wander. If the first inequality is not satisfied, then the time resolution of the data is

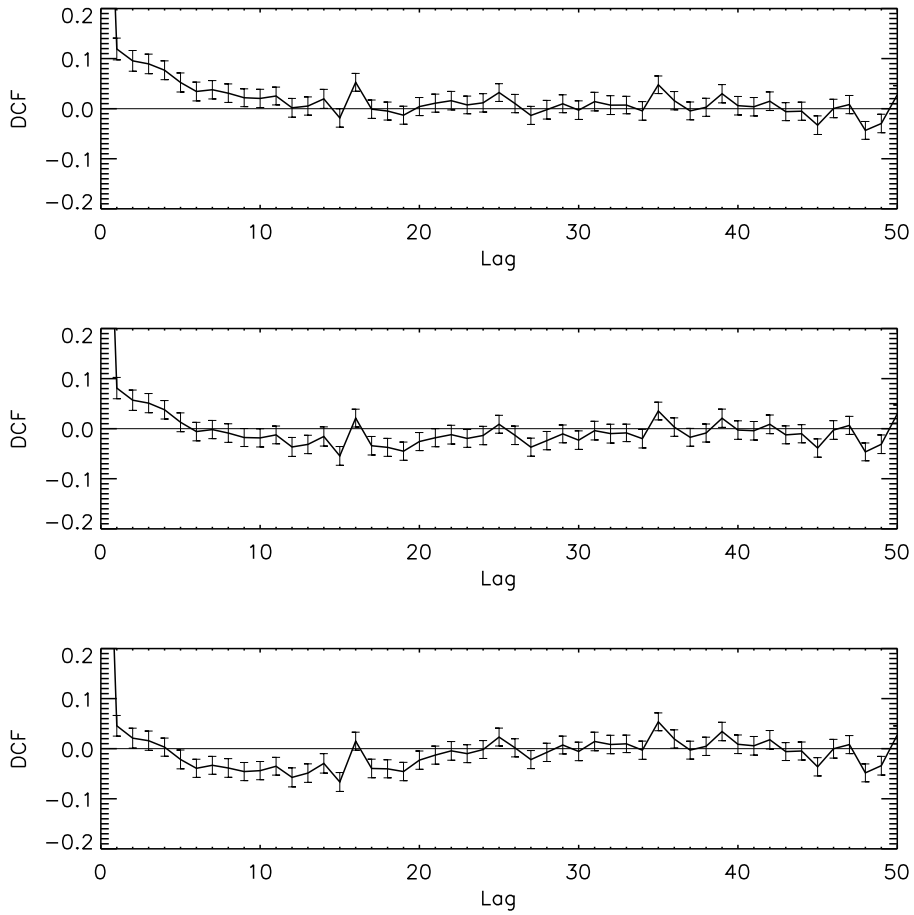

Figure 19. DCFs for whitened simulated residuals using $W = 75, 50, 25$, after adding a "sawtooth" function to the simulated residuals shown in Figure 6. The relaxation timescale of 10 units is easily identified for $W = 75$, with low-frequency wander nearly completely subtracted by the high-pass filter. For $W = 50$, the fitting function begins to subtract the correlations. At $W = 25$, the time series is overwhitened, resulting in reduction of the relaxation signature and anticorrelations from lags of $\sim 5 - 25$.

not sufficient to resolve the correlation timescale. If the second condition is not met, then the correlation cannot be disentangled from the wander.

Lagged Dispersion. As another statistic to measure correlations, we define the *lagged distribution function*, $LDF\{\delta t, \tau\}$, the distribution of fluctuation *differences* separated in time by a lag τ. We denote the dispersion of $LDF\{\delta t, \tau\}$ as $LD(\tau)$. The LD has the following properties for a data set that is correlated over a timescale τ_c (and without a resonance). Because the time series will resemble itself to some extent upon time translation by times $\tau < \tau_c$, the $LDF\{\delta t, \tau\}$ will be relatively narrow, and hence $LD(\tau)$ will be relatively small. For $\tau > \tau_c$, the dispersion is larger because the data around time $t + \tau$ are uncorrelated with the data around time t; in this case $LDF\{\delta t, \tau\}$ is broader than at low lag, and $LD(\tau)$ asymptotes to some maximum value as τ is increased. If the data series is simply noise, there will be no statistically-significant variations in $LD(\tau)$ with τ, since the data contain no timescale. Hence, our approach is to look for statistically-significant variations in $LD(\tau)$ as τ is increased.

To account for unequal sampling, we construct $LD(\tau)$ in the same way as the $DCF(\tau)$:

$$LD(\tau) \equiv \frac{1}{M-1} \sum (\Delta t_{ij} - \overline{\Delta t})^2, \tag{3.14}$$

where, as before, the sum is over the set of M elements that satisfies Eq. (3.10), in which each element of the set is associated with the lag value τ. The mean $\overline{\Delta t}$ in Eq. (3.14) is defined as

$$\overline{\Delta t} \equiv \frac{1}{M} \sum \Delta t_{ij}. \tag{3.15}$$

The standard uncertainty in $LD(\tau)$ follows the same form as for the DCF, and is

$$\sigma_{LD}(\tau) = \frac{1}{M-1}\left[\sum(\Delta t_{ij} - \overline{\Delta t})^2 - LD(\tau)\right]^{1/2}. \quad (3.16)$$

The LD for the simulated sawtooth function shown in Figure 18 is shown in Figure 20. To assess the statistical significance of these results, we decorrelated the data through random shuffling of the points. For 100 such shufflings, we calculated the average $LD(\tau)$ to establish the base $LD(\tau)$ one would expect under the null hypothesis that the data are completely uncorrelated; these values are shown as the horizontal lines in each figure, $LD(\tau)$ is normalized in terms of this average value. This method has the advantage that nothing is assumed about the underlying statistics of the data, rather, the data themselves are used to evaluate $LD(\tau)$ for the null hypothesis. The LD reveals that the data are correlated over a timescale of 10 time units, consistent with results of the DCF for this simulated time series (Figure 19).

3.3. Data

We have applied our analysis techniques to the 32 radio pulsars of Table 2. In this section, we show results of our analysis applied to data for PSRs B0525+21, B1556-54, B0950+08, B1133+16, and B1933+16 as particularly interesting examples.

3.3.1. PSR B0525+21

For several objects, we find no evidence, or marginal evidence for correlation timescales. Timing residuals for PSR B0525+21 are shown in Figure 21 (top panel). The wander in the timing noise occurs over timescales $\gtrsim 300$ days. Upon whitening

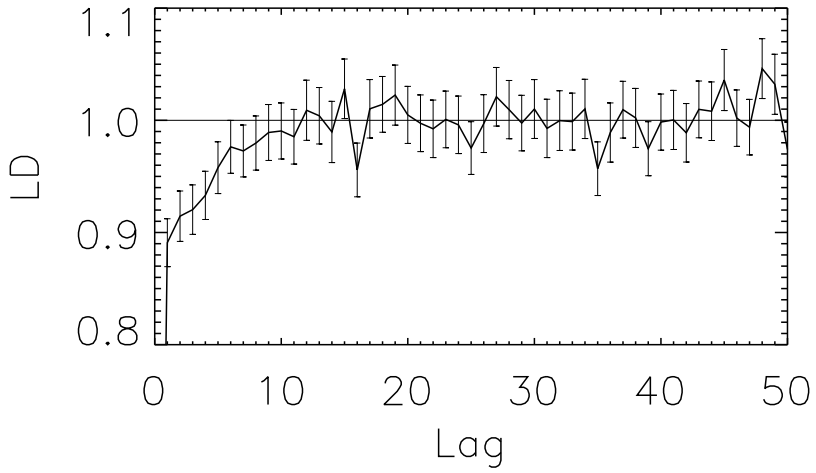

Figure 20. LD of the time series shown in Figure 18, after whitening with $W = 75$. The relaxation process occurring over 10 time units is evident, confirming the results of the DCF shown in Figure 19.

Name	Name
B0136+57	B1642-03
B0329+54	B1749-28
B0355+54	B1818-04
B0525+21	B1822-09
B0628-28	B1831-03
B0736-40	B1859+03
B0740-28	B1911-04
B0818-13	B1919+21
B0823+26	B1929+10
B0835-41	B1933+16
B0950+08	B1946+35
B1133+16	B2016+28
B1237+25	B2020+28
B1508+55	B2045-16
B1556-44	B2111+46
B1641-45	B2217+47

Table 2. Complete list of pulsars which we have studied using the analysis techniques described in this chapter.

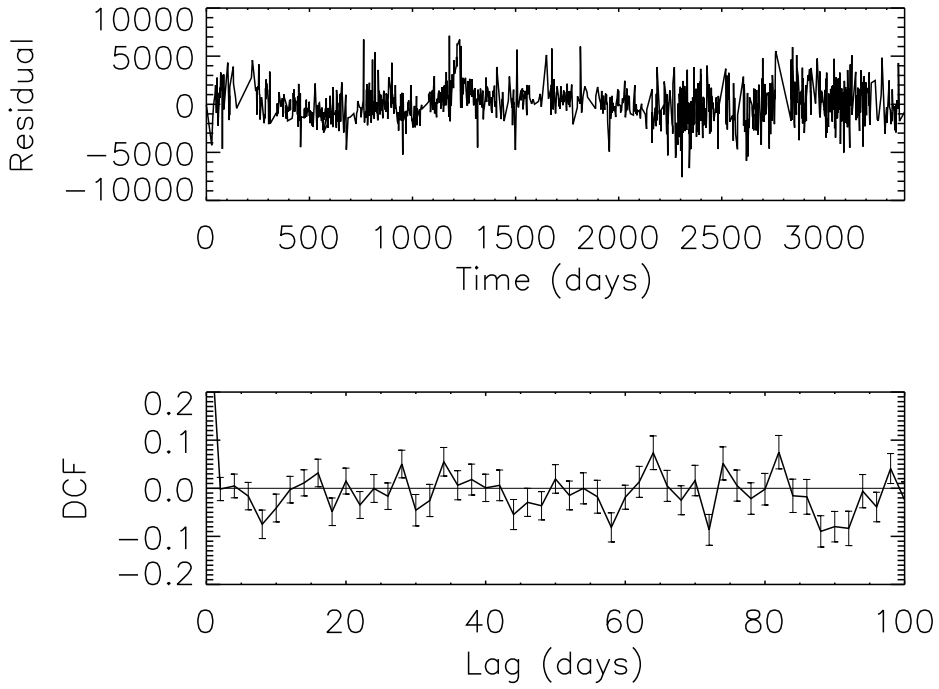

Figure 21. Top panel - Timing residuals for PSR B0525+21, in microseconds. Bottom panel - DCF of PSR B0525+21 residuals after whitening with $W = 100$ days. There is marginal evidence for quasi-periodicity.

with a boxcar width $W = 100$ days, the DCF (bottom panel) shows marginal evidence for quasi-periodicity.

3.3.2. PSR B1556-54

Some pulsars show large amplitude wander over timescales shorter than 100 days, such as PSR B1556-54. Timing residuals are shown in Figure 22 (top panel). DCFs for this object are shown in Figure 22 for $W = 100$ (middle panel) and 50 days (bottom panel). For $W = 100$ days, the DCF shows quasi-periodic oscillations, possibly due to

magnetospheric changes. With $W = 50$, more wander is removed, but quasi-periodic oscillations are still evident (bottom panel).

3.3.3. PSR B0950+08

Timing residuals for PSR B0950+08 are shown in Figure 24. The DCF reveals periodic wander on short timescales, similar to that seen in PSR B1556-54 (Figure 23). However, the pulse profile for this object is known to change from one "mode" to another over similar timescales to those identified in the DCF (Shabanova & Shitov 2004). Correlations observed for this object may be due to changes in the magnetosphere which also affect the pulsar beam (Lyne et al 2010).

3.3.4. PSR B1133+16 and PSR B1933+16

We now focus on PSR B1133+16 and B1933+16, two particularly interesting pulsars. Our analysis reveals strong evidence of a relaxation process.

Aside from being one of the brightest radio pulsars in the northern hemisphere, the characteristics of PSR B1133+16 are typical for an old pulsar. It has a spin period of 1.19 s, an inferred dipole magnetic field of $\simeq 2 \times 10^{12}$ G, and the spin-down age is $\simeq 5 \times 10^6$ yr. 4000 days of timing residuals for PSR B1133+16 are shown in Figure 25 (top panel). These data were obtained by the 12.8 m telescope at Jodrell Bank, with monitoring nearly daily, usually at 610 MHz.

PSR B1933+16 is also unremarkable in most parameters, with a spin period of 0.36 s, an inferred dipole field of $\sim 10^{12}$ G, and spindown age of $\sim 9 \times 10^5$ yr.

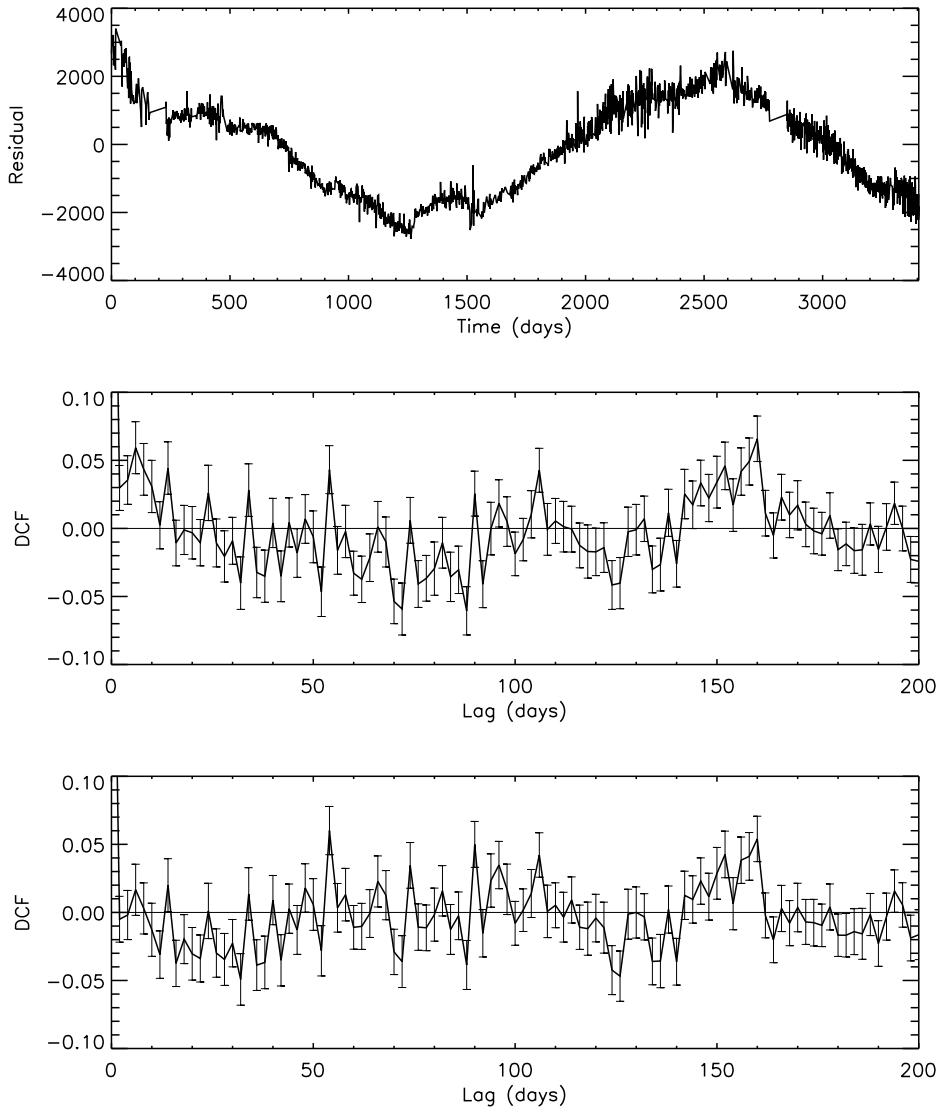

Figure 22. Top panel - Timing residuals for PSR B1556-54. Middle panel - DCF for PSR B1556-54, using $W = 100$ days. Quasi-periodic fluctuations are evident. Bottom panel - DCF for PSR B1556-54, using $W = 50$ days. More wander has been removed, but some quasi-periodicity is still evident.

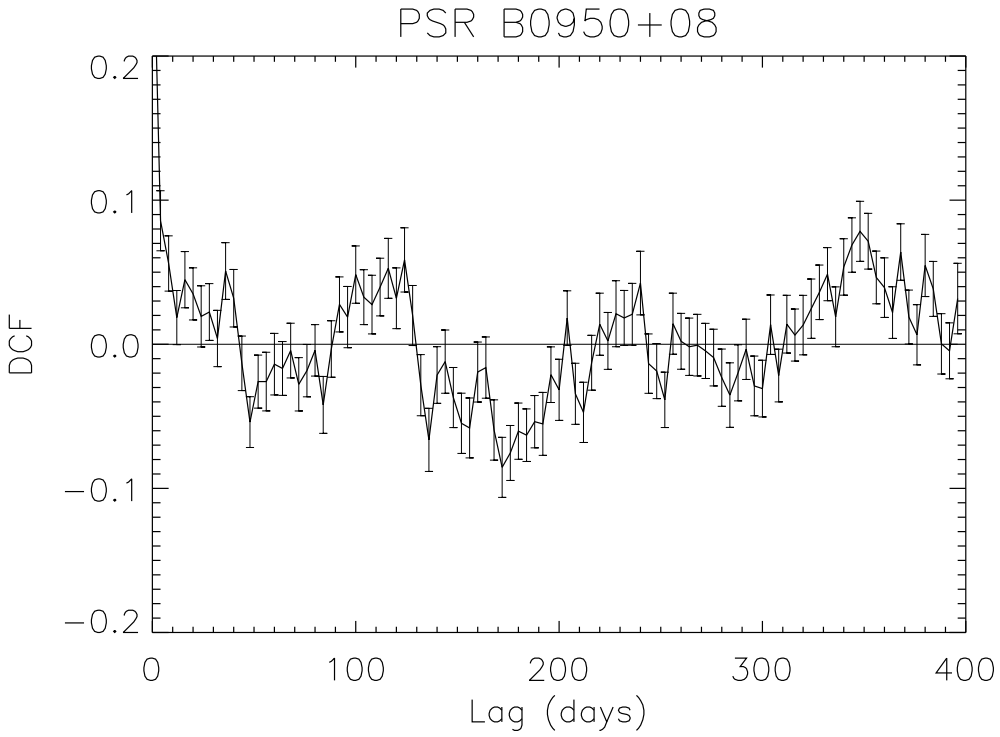

Figure 23. DCF for PSR B0950+08. This behavior may be due to torque variability caused by changes in the magnetosphere. Our techniques allow us to distinguish this behavior from relaxation processes.

Approximately 6000 days of timing residuals for PSR B1933+16 are shown in Figure 26 (top panel). These data were also obtained by the 12.8 m telescope at Jodrell Bank, with monitoring almost daily, usually at 610 MHz.

In Fig. 27 we show the DCFs for B1133+16 and B1933+16, where the error bars were obtained from Eq. (3.12). (All error bars in this chapter are 1-σ). The DCF for B1133+16 shows highly significant, non-periodic correlations over a timescale $\tau_c \sim 10$ d, with the distinct structure of a relaxation process. B1933+16 shows similar correlations, over a timescale $\tau_c \sim 40$ d. To determine the significance of the correlation signature in the DCF for each object, we shuffle the whitened residuals

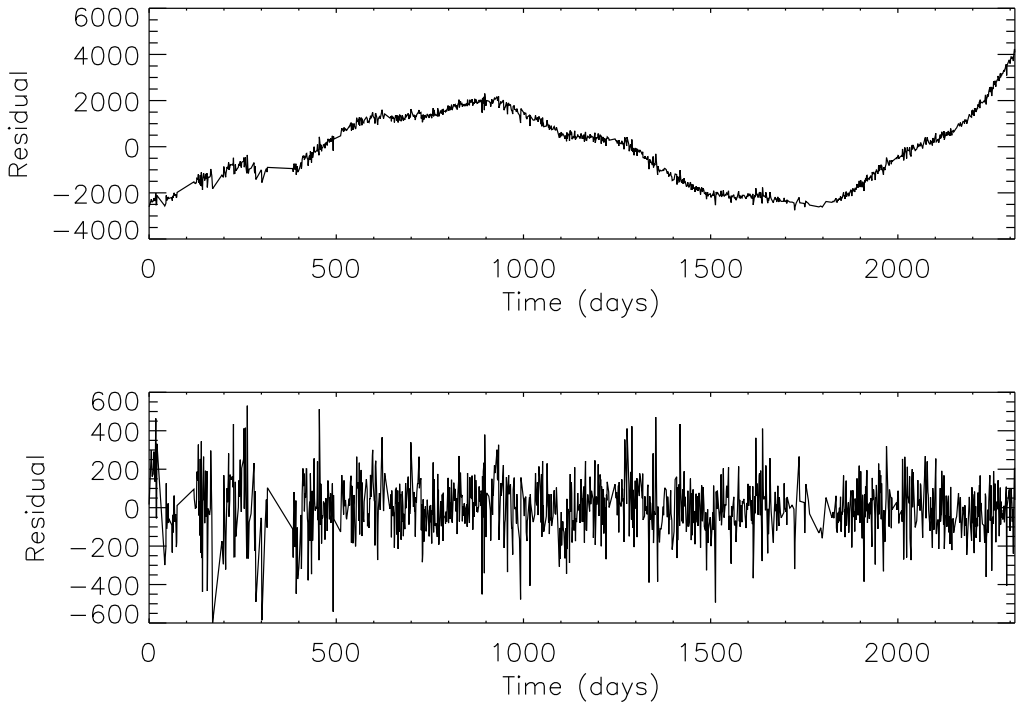

Figure 24. Timing residuals for PSR B0950+08, in microseconds. Timing residuals are shown before whitening in the upper panel, and after whitening with a boxcar width $W = 100$ days in the lower panel.

randomly in time and calculate the correlation significance $DCF(\tau)/\sigma(\tau)$ for each data point. The total correlation significance for each object is

$$S = \prod_i \frac{DCF(\tau_i)}{\sigma(\tau_i)}, \tag{3.17}$$

where the sum is over all values of $\tau_i < \tau_c$, the inferred correlation timescale. If the correlation significance of the unshuffled data is less than that for the shuffled data, we conclude that the correlation is statistically insignificant. In 10,000 such shufflings for each data set, the null result is never realized. We therefore estimate

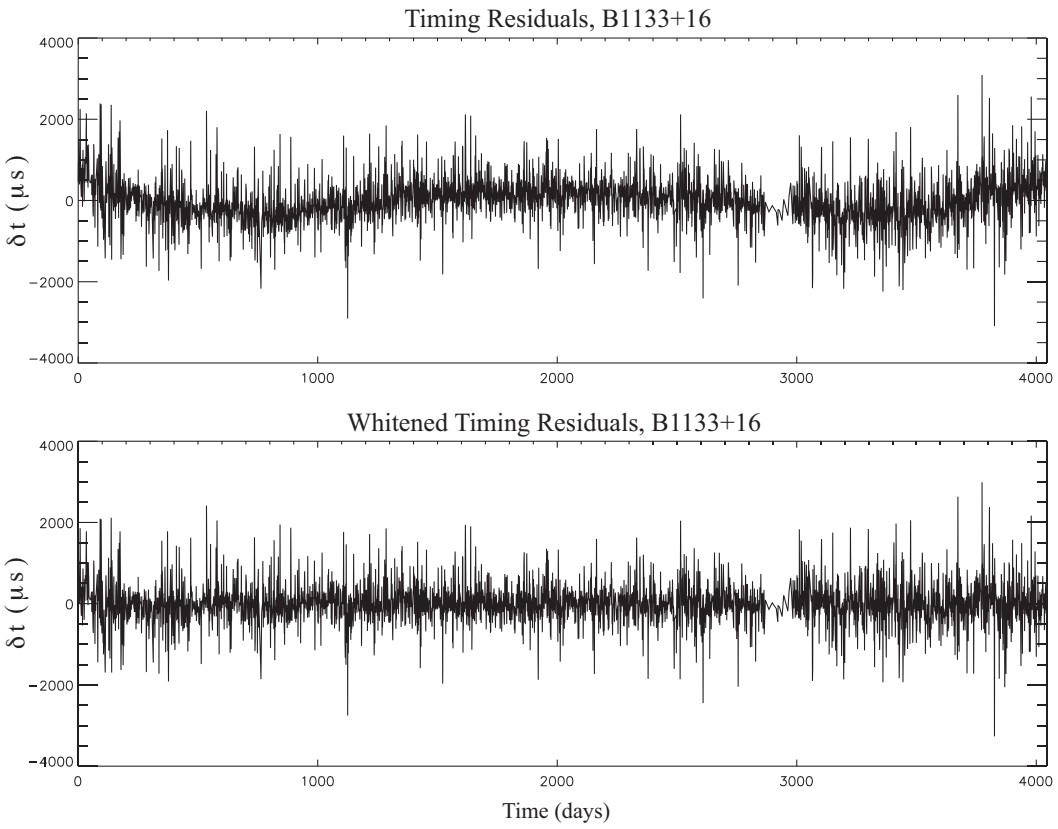

Figure 25. Timing fluctuations in PSR B1133+16. The bottom panel shows the residual timing fluctuations after subtraction of the long-term wander evident in the top panel. The uncertainties are comparable in magnitude to the fluctuations, and are not shown for clarity. The gaps in the data sets are on account of equipment upgrades; our analysis techniques enable us to use data on both sides of the gaps..

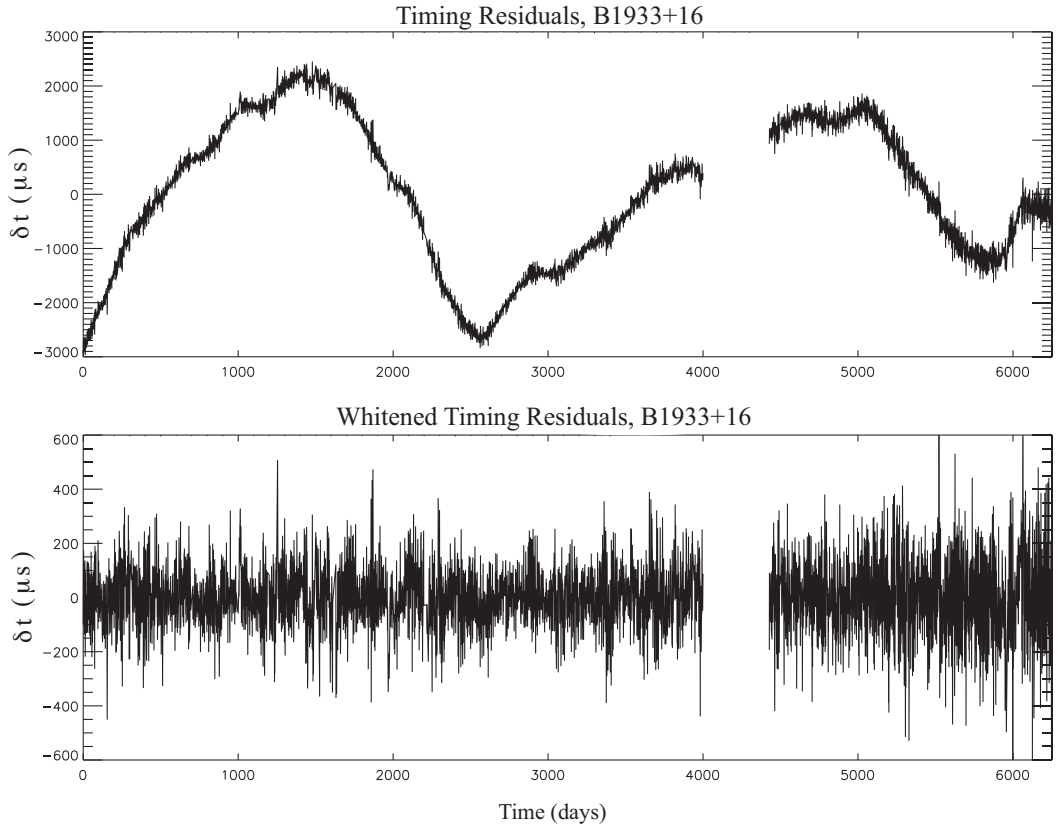

Figure 26. Timing fluctuations in PSR B1933+16. The bottom panel shows the residual timing fluctuations after subtraction of the long-term wander evident in the top panel. The uncertainties are comparable in magnitude to the fluctuations, and are not shown for clarity. The gaps in the data sets are on account of equipment upgrades; our analysis techniques enable us to use data on both sides of the gaps.

the statistical significance of the detected correlations to exceed $1 - 10^{-4}$, consistent with the uncertainties given in Figure 27.

In Figure 28 we show $LD(\tau)$ for each pulsar. We see lower dispersion out to a lag of ~ 10 d for B1133+16, and ~ 40 d for B1933+16. For B1133+16, we find that $LD(\tau)$ is significantly lower than what we expect from the null hypothesis out to

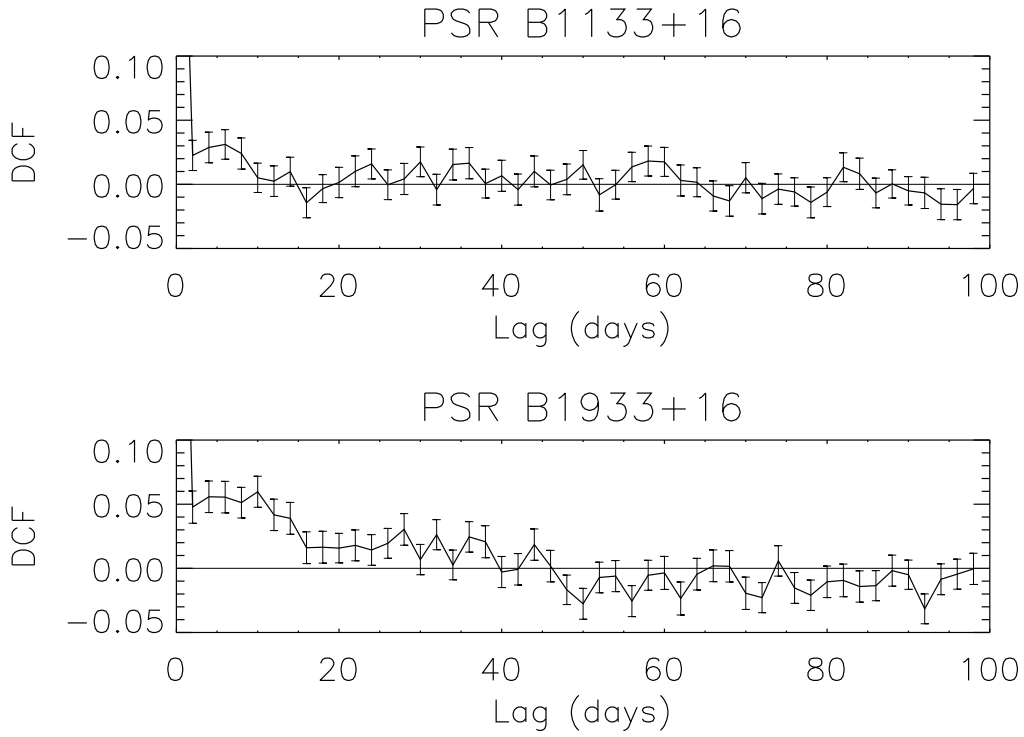

Figure 27. The DCF of the two time series in Figures 25 and 26 (bottom panels) For B1133+16, we use $W = 400$. For B1933+16, $W = 120$.

$\tau \simeq 10$ d, in support of the DCF result. B1933+16 is very similar, but indicates a relaxation timescale $\tau \simeq 40$ d, as in the DCF.

The power spectra of these objects do not show the correlations that our time-domain analysis has revealed. Gaps in observations of 4-5 days are frequent for B1133+16, and several gaps of 8-16 days are present. To obtain a power spectrum without interpolating data, we have chosen a span of data approximately 1700 days in length, with gaps no longer than 4 days. The power spectrum of the timing residuals are shown in Figure 29 (top panel), using 4 day binning with uniform weighting. The spectrum indicates that the signal is composed of white noise, with excess power

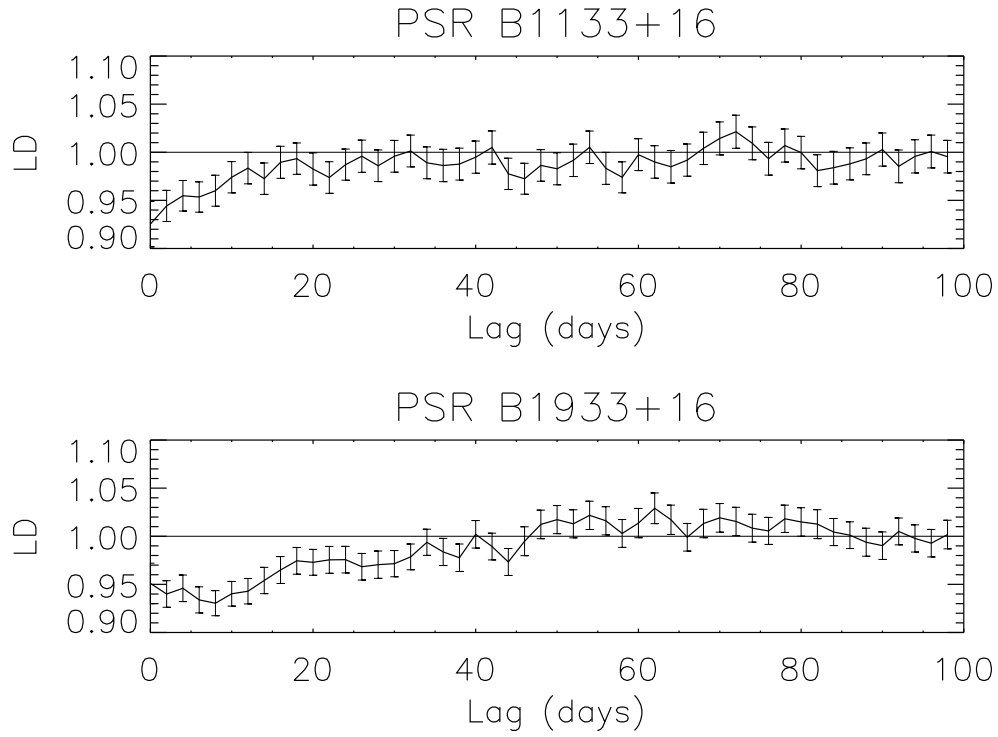

Figure 28. Dispersion of the lagged distribution function (LD), normalized by its average value for many shufflings of the time series. The curve corresponds to the data, while the horizontal line corresponds to the dispersion of the data under the null hypothesis of no correlations (see text). As with the DCFs, $W = 400, 120$ for B1133+16 and B1933+16, respectively.

at low frequencies. No high frequency features or spectral breaks are evident. For PSR B1933+16, we select a section of data spanning 1400 days to analyze with Fourier techniques, following the technique described for PSR B1133+16. The data are binned to 4 day wide bins, with the resulting power spectrum shown in Figure 29 (bottom panel). The red spectrum corresponds to the low-frequency wander visible in the timing residuals (Figure 26).

In Figure 30 we show the probability distribution functions of the fluctuations about the mean, $PDF\{\delta t\}$ for B1133+16 and B1933+16. Interestingly, the time series

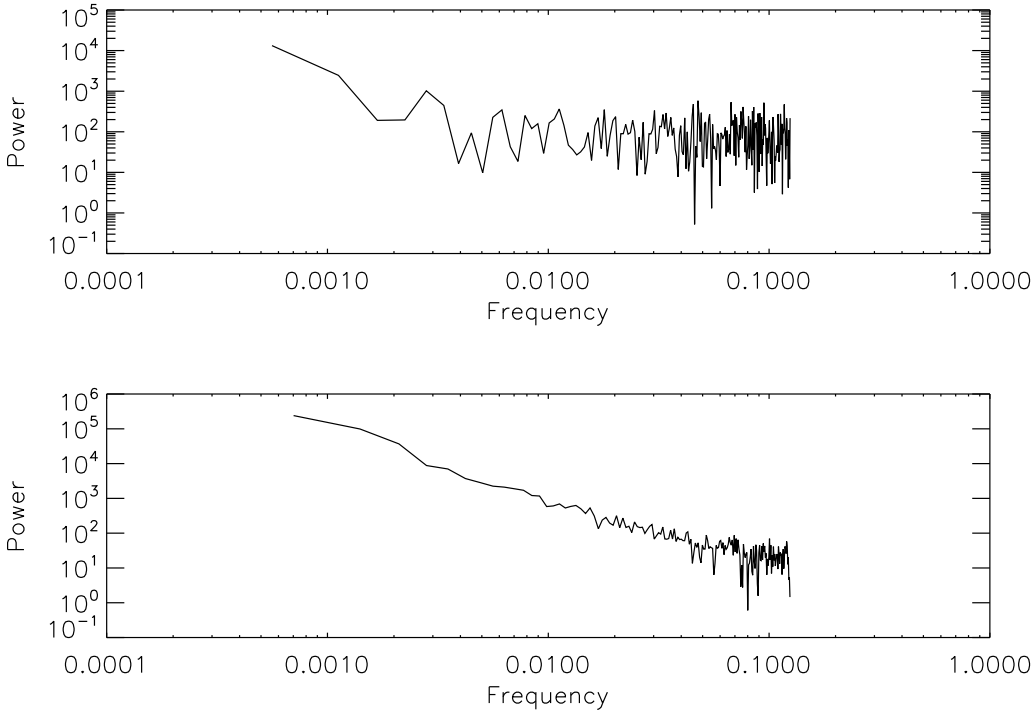

Figure 29. Top panel - Power spectrum of B1933+16 residuals. Bottom panel - Power spectrum of B1933+16 residuals. No frequency dependent structure is evident.

of neither pulsar is well-described by a random Gaussian process. This is especially striking for B1133+16, whose distribution falls somewhere between a Gaussian and a Cauchy-Lorentz distribution.

3.4. Robustness Tests

To ensure that the correlations found using the DCF are not introduced by the whitening method, we compare our results to those found using other techniques, using PSR B1133+16 for illustration. In the case of this object, the wander in the timing noise can be well removed with a 5th order polynomial. Applying the DCF

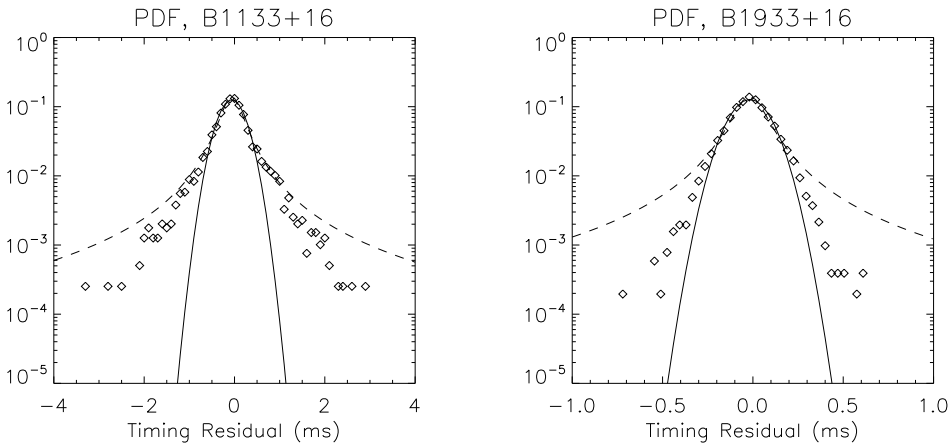

Figure 30. PDFs of observed fluctuations in pulse arrival times after high pass filtering, corresponding to data sets in Figures 25 and 26 (bottom panels). We also show the best fits of Gaussian (solid line) and Cauchy-Lorentz (dashed line) functions.

analysis to the data whitened using this technique, results are very similar to those we find using the technique described in Section 3.3 (Figure 31 middle panel). We also apply the DCF to unwhitened data for PSR B1133+16, and then whiten the correlation function, rather than the time series, to remove the signature of low-frequency wander from the DCF. Results using this technique for PSR B1133+16 are shown in the bottom panel of Figure 31. These three whitening techniques give nearly indistinguishable results.

A large difference in timescales exists for B1133+16 between the relaxation timescale ($\sim$ 10 d) and the characteristic wander ($\sim$ 1000 d). This allows a wide range of high-pass filter widths W for which our results remain unchanged. The wander is not well removed for $W \gtrsim 600$ days, and the fitting function begins to subtract the relaxation

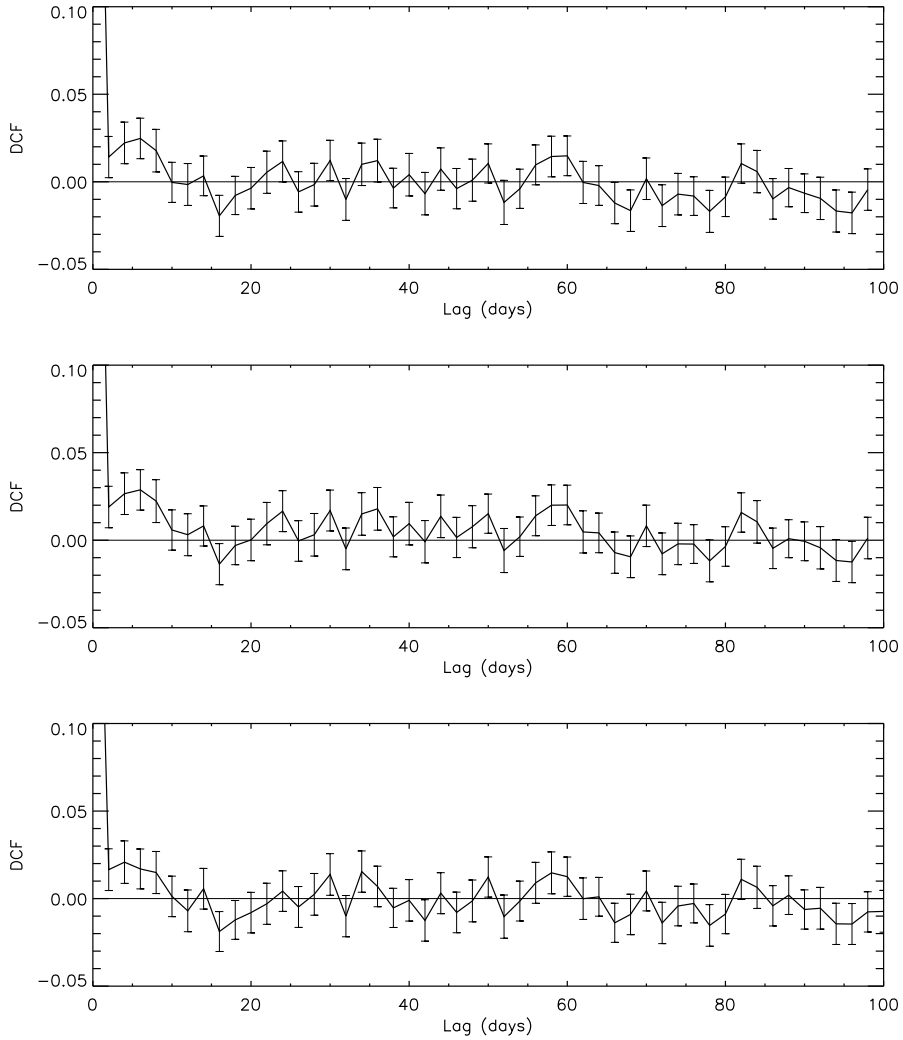

Figure 31. DCF for PSR B1133+16, using three different whitening methods. In the top panel, the whitening method described in section 3.3 is used. For the middle panel, timing residuals were whitened using a fifth-order polynomial. For the bottom panel, the DCF function itself was whitened (see text).

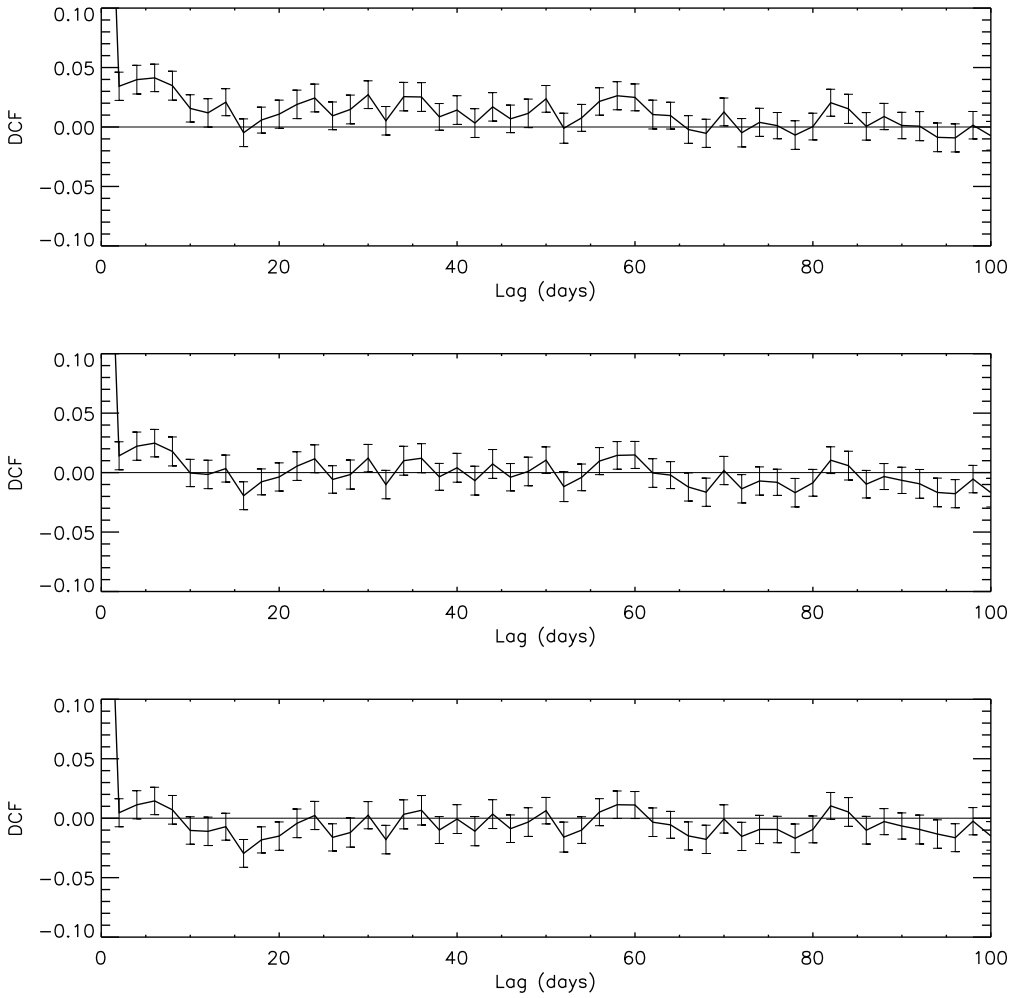

Figure 32. DCFs for PSR B1133+16 for several values of W. Top panel - $W = 600$ days. Middle panel - $W = 200$ days. Bottom panel - $W = 80$ days. For $W \sim 100-500$ days, the DCFs are nearly indistinguishable.

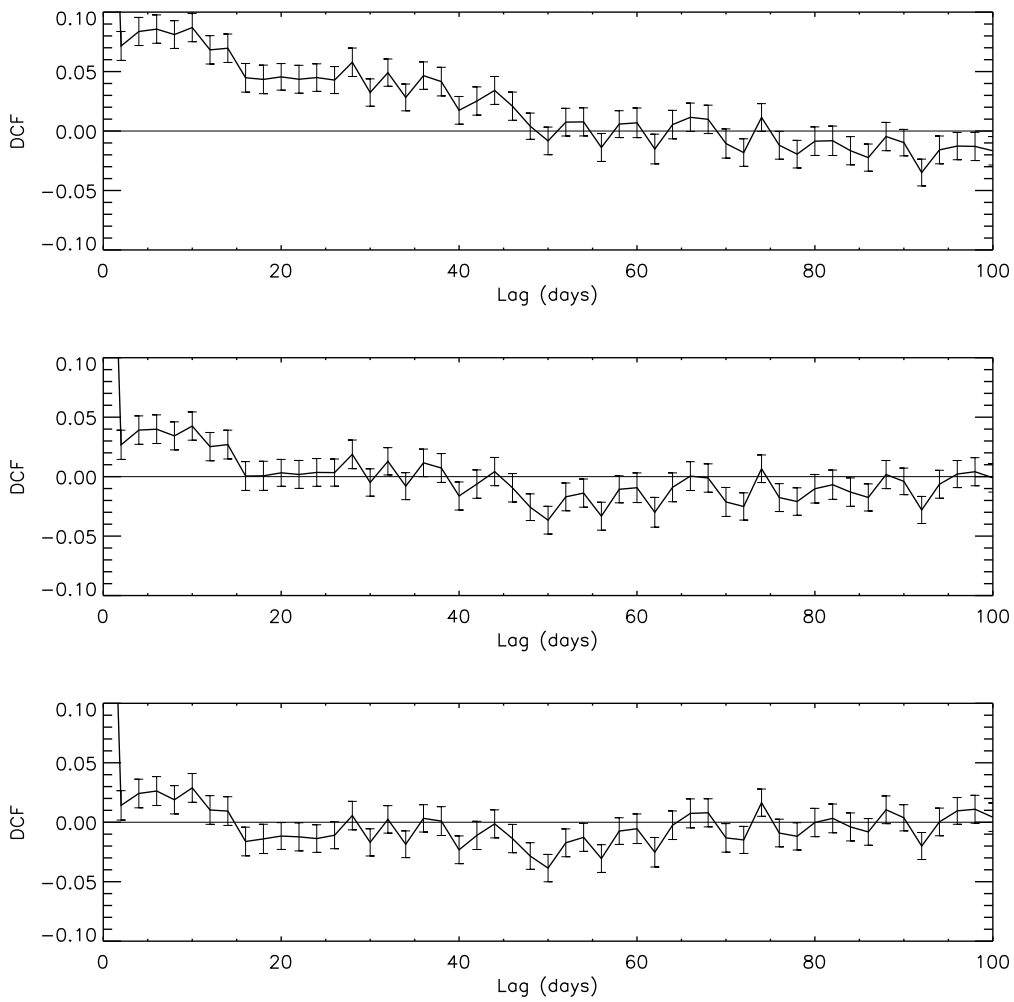

Figure 33. DCFs for PSR B1933+16 for several values of W. Top panel - $W = 140$ days. The wander is not yet completely removed. Middle panel - $W = 100$ days. This time series is properly detrended. Bottom panel - $W = 60$ days. This time series has begun to be overdetrended, though positive correlations for $\tau < 20$ are clear. For $W \sim 80 - 120$ days, the DCFs are nearly identical.

correlations for $W \lesssim 100$ days. We show DCFs for PSR B1133+16 for several values of W in Figure 32.

The characteristic timescale of the wander is much shorter for B1933+16, ~ 300 d. We plot several DCFS for B1933+16 for different values of W (Figure 33). In

order to successfully remove the wander, W must be a factor of smaller than the shortest characteristic timescales of the wander. We also ensure that W is a factor of 2-3 higher than the relaxation timescale we identify for each object. In the case of B1933+16, this leaves little room to vary W. To reveal the relaxation timescales shown in Figures 27 and 28, we use a cutoff frequency of 400 days^{-1} for B1133+16, and 120 days^{-1} for B1933+16.

3.5. Discussion

The two complementary and independent statistics, $DCF(\tau)$ and $LD(\tau)$, that we have used here measure different properties of the data. The DCF measures the extent to which the data resemble themselves upon translation in time, while the LD measures the extent to which the PDF of fluctuation differences widens as the data decorrelate upon translation in time. The shape of the DCF also indicates the form of the correlation. That these different statistics give the same results gives us confidence that we have identified correlations in both data sets. The correlation found in B1133+16 cannot be an artifact of the whitening process. The characteristic timescale of the whitening function was ~ 500 d, and its subtraction could not introduce spurious correlations over a time scale as low as $\sim \tau_c$, nearly two orders of magnitude shorter.

We consider it unlikely that correlations we have detected are due to mode changes in the pulsar magnetosphere of the kind identified by Lyne et al. (2010). PSR

B1133+16 and PSR B1933+16 show no evidence for such modes changes. Moreover, timing correlations due to mode changes would show both correlations and anti-correlations, while B1133+16 and B1933+16 show only correlations. Timing residuals for PSR B0950+08, a pulsar known to exhibit mode changes (Shabanova & Shitov 2004), are shown in Figure 24. Upon whitening the data, the DCF of this object reveals both correlations and anti-correlations (Figure 23). This may be evidence of magnetospheric effects contributing to timing noise. Our analysis techniques afford a powerful method with which to differentiate between this behavior and relaxation processes in the star.

The correlations also cannot be due to time variability of the interstellar medium. The delay in the arrival time of a pulse of frequency ν_{MHz} due to dispersion in the interstellar medium is (Lyne & Graham-Smith 2005)

$$\Delta t_{ISM} = 4.15 \times 10^6 \,\mathrm{MHz}^2 \,\mathrm{pc}^{-1} \,\mathrm{ms} \times \nu_{\mathrm{MHz}}^{-2} \times \mathrm{DM}, \tag{3.18}$$

where DM is the dispersion measure (cm^{-3} pc). The dispersion measure is calculated during multi-wavelength observations for B1133+16 and B1933+16, and used to subtract the delay as part of the timing model. Long term monitoring of these pulsars allows calculation of the time derivative of the dispersion measure, $d(DM)/dt \sim 8 \times 10^{-4} \mathrm{cm}^{-3} \,\mathrm{pc}\,\mathrm{yr}^{-1}$ for B1133+16, and $\sim 2.3 \times 10^{-3} \,\mathrm{cm}^{-3} \,\mathrm{pc}\,\mathrm{yr}^{-1}$ for B1933+16 (Hobbs et al. 2004). This variability of the electron density produces small fluctuations in the arrival time delay, on the order of $10\,\mu\mathrm{s}\,\mathrm{yr}^{-1}$. To estimate the maximum effect of variations of the interstellar medium, we superimposed a sine

wave of amplitude $10\mu s$ with period 10 d on our whitened data. No detectable signal is introduced into either the DCF or the LD.

For most of the pulsars in Table 2, we find no evidence of relaxation behavior. we find no evidence of non-periodic correlations over short timescales. We have identified several factors that could inhibit detection. Some of the objects we have analyzed have been observed on a weekly basis. In order to resolve correlation timescales of $\sim$ 10 d, we find that nearly daily sampling is required. In addition, many data sets have an insufficient number of points to enable us to make an identification of any correlations. We estimate that to successfully identify non-periodic short-timescale correlations in inherently noisy pulsar timing data, it is necessary to monitor objects nearly daily for 10 years or longer. For data which contain relaxation and periodicity over similar timescales, it is not possible to remove the wander without removing any non-periodic correlations that may exist.

We interpret the correlations found in PSRs B1133+16 and B1933+16 as evidence of a damped rotation mode that is frequently excited by the noise process. This is the first evidence for differential rotation apart from glitches, a result that supports the expectation that most of the neutron star interior is a fluid. This discovery was made possible with 1) high-resolution data collected over decades, only possible now, 2) proper whitening of the timing residuals, as developed in this thesis, and 3) analysis of the data in the time domain.

The analysis methods described in this chapter may be usefully applied to other data analysis problems. Our techniques are well suited for seeking time correlated structure in noisy time series. In particular, our methods may be used to detect timing noise fluctuations due to magnetospheric effects, such as those described by Lyne et al. (2010). These techniques may also be used to detect precession and oscillation modes in pulsar timing data. We hope introduction of these methods will stimulate research in this area, and motivate further high resolution monitoring of pulsars.

4. NEUTRON STAR THERMAL AND MAGNETIC EVOLUTION

In this chapter, we review the factors that determine the thermal and magnetic evolution of neutron stars. We discuss relevant cooling processes at early and late thermal times, and review several possible internal heating mechanisms. We outline several factors that may lead to evolution of the magnetic field on timescales short compared to the observable lifetime of a neutron star.

4.1. Thermal Evolution

At the time of its formation, the temperature of a neutron star is $\sim 10^{11}$ K. Subsequent cooling is determined by neutrino emission from the interior and photon emission from the surface. Within just a few days, neutrino emission cools the star to below 10^{10} K. Neutrinos continue to dominate the cooling trajectory for $\sim 10^4$ years, at which time the interior of the star reaches an isothermal state. At a characteristic age of $\sim 10^5$ years, cooling is dominated by photon emission from the surface. Heat is liberated from the core by conduction through the outer layers of the star. Assuming no heat sources in the stellar interior, the surface temperature and the core temperature are closely tied, following the approximate relation (Gudmundsson et al. 1982)

$$T_{b8} = 1.288 \left(\frac{T_{s6}^4}{g_{s14}} \right)^{0.455}, \tag{4.1}$$

where T_{b8} is the temperature at the base of the crust in units of 10^8 K, T_{s6} is the surface temperature in units of 10^6 K, and g_{s14} is the surface gravity in units of $10^{14}\,\mathrm{cm\,s^{-2}}$.

The precise trajectory of a neutron star's temperature evolution depends on the composition of the interior, relevant cooling processes, and heating processes (if any). Neutrino emission is dominated by Urca processes, during which particles emit neutrinos by beta decay and inverse beta decay. The direct Urca process is the most efficient for cooling the neutron star core, given by

$$n \rightarrow p + e^- + \bar{\nu}_e, \tag{4.2}$$

$$p \rightarrow n + e^+ + \nu_e. \tag{4.3}$$

The proton to neutron ratio determines whether the direct Urca process is attainable, or whether the much less efficient modified Urca process operates, given by

$$n + (n,p) \rightarrow p + (n,p) + e^- + \bar{\nu}_e, \tag{4.4}$$

$$p + (n,p) \rightarrow n + (n,p) + e^+ + \nu_e. \tag{4.5}$$

Additionally, the existence of superfluidity suppresses neutrino emission at early times by limiting the effectiveness of Urca processes, and enhances cooling at later times by lowering the specific heat (Maxwell 1979).

Sources of internal heating may include friction between the crust and superfluid components and decay of the magnetic field. As we illustrated in section 2.1, fluid components in the interior may rotate at a different rate than the crust, resulting in

heat generation from friction between the two components. Ohmic dissipation of the magnetic field may also be a relevant heating process in the crusts of neutron stars, where the electrical conductivity is orders of magnitude lower than in the core. Field decay may be especially important in highly magnetized neutron stars. Kaminker et. al (2006) find that standard cooling models significantly underestimate the surface temperature of such stars (Figure 34). They conclude that a heating layer near the base of the outer crust is consistent with the observed temperatures of magnetars. Such heating could be produced by ohmic decay of strong magnetic fields found in magnetars, thus coupling their thermal and magnetic evolution.

4.2. Magnetic Fields

The magnetic field is the distinguishing feature of a neutron star, dividing millisecond pulsars from standard pulsars, and quiescent emitters from bursters. The field is born, or rather reborn, during the supernova event that produces the neutron star. As the progenitor star collapses, the magnetic flux already present is unable to be expelled from the star due to flux freezing. Currents that exist in the interior cannot decay quickly because the induced EMF produced by a change in the current works to support the existing current, similar to a simple R-L circuit. The decay time of such a circuit is very long, thus keeping the magnetic flux constant even in a plasma. The neutron star has a radius $\sim 10^5$ times smaller than the main sequence star from which it was born. Because the flux is held constant during collapse, the

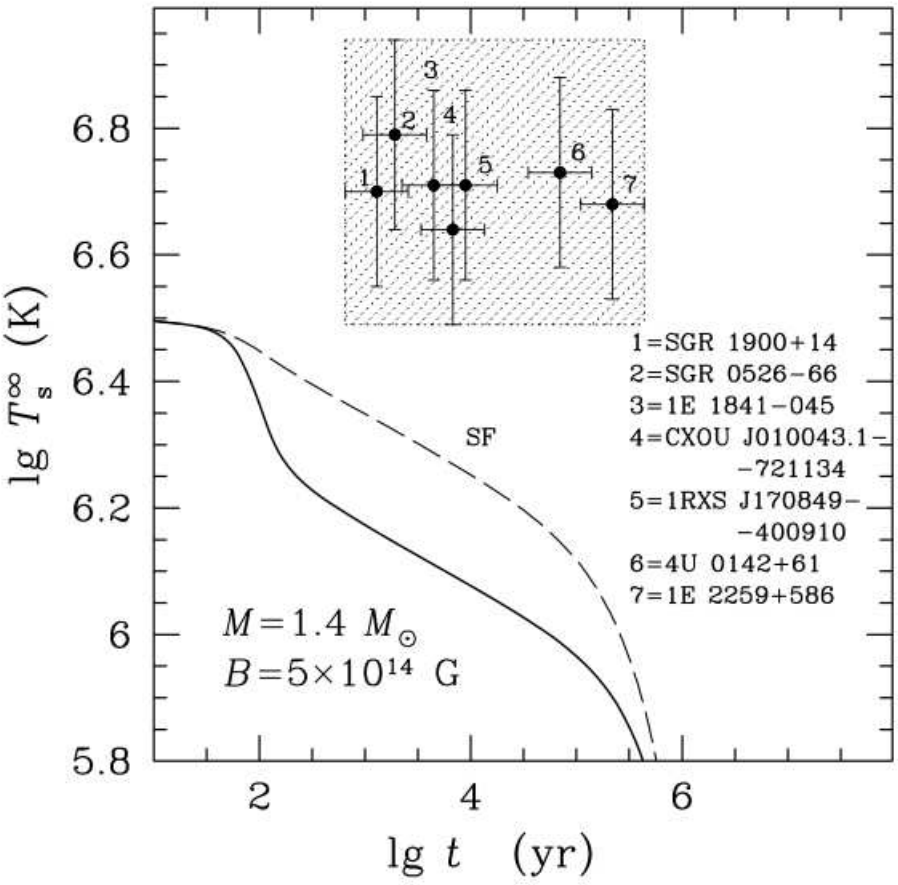

Figure 34. Observed magnetar surface temperature vs. age. The solid line represents a standard cooling model with no superfluidity, the dashed line included proton superfluidity in the core. From Kaminker et al. (2006) .

magnetic field is $\sim 10^{10}$ times larger. For a typical giant star with magnetic field strength $\sim$ 100 G, this produces a $\sim 10^{12}$ G neutron star. In magnetars, the initial field strength may be augmented by a dynamo process soon after neutron star formation (Thompson & Duncan 1993).

The global structure of the magnetic field is likely composed of poloidal and toroidal components. Magnetic field models indicate that the poloidal component,

inferred from spin-down measurements, may be smaller than the toroidal component by an order of magnitude (Braithwaite 2009). The recent discovery of a Soft Gamma Repeater with a relatively small ($B < 7.5 \times 10^{12} G$) dipole field supports this idea. SGR 0418+5729 was discovered in 2009 after emitting two magnetar-like bursts (van der Horst et al. 2010), after which it became detectable as a pulsating source of X-rays. Spin-down measurements indicate that the emission cannot be powered by decay of the dipole field, but must rely on a very large ($< 10^{16} G$) internal field as a source of energy (Dall'Osso et al. 2011).

Estimates of the magnetic field strengths in young and old pulsars indicate that the field evolves over timescales short compared to a neutron star's observable lifetime. For a model in which charged particles move due to electromagnetic forces relative to a neutral background, evolution of the magnetic field in the core is governed by the equation (Goldreich & Reisenegger 1992)

$$\frac{\partial \mathbf{B}}{\partial t} = \nabla \times (\mathbf{v} \times \mathbf{B}) + \gamma \nabla \times \left(-\frac{\mathbf{j}}{n_e e} \times \mathbf{B} \right) - \nabla \times \left(\frac{c}{\sigma} \mathbf{j} \right), \tag{4.6}$$

where $\mathbf{v}$ is the weighted average velocity of charged particles, $\mathbf{j}$ is the electric current, n_e is the number density of electrons, e is the elementary charge, σ is the conductivity, and γ is a dimensionless factor that parameterizes the coupling between the charged particles and the neutral background. The terms on the right hand side correspond to physical processes, known as ambipolar diffusion, Hall drift, and ohmic diffusion (from left to right).

Ambipolar diffusion allows the magnetic field to move through a flow of the charged particles to which the field is coupled, due to bouyancy-like forces. This process is not likely to be effective in normal neutron stars, as it creates chemical potential gradients that quench the bulk flow (Reisenegger 2003). However, in strongly magnetized neutron stars, this process can cause a flow of charged particles along with the magnetic field from the core to the crust/core boundary. The Hall drift term is not dissipative in itself, but can lead to small scale structures in the magnetic field. Magnetic structures with smaller scales decay faster under the influence of ohmic diffusion, the familiar dissipative term resulting from resistivity of a medium to the flow of charged particles. Ohmic diffusion has a very long decay timescale for typical neutron star parameters, so is not likely to have a large effect on the global field. The decay time due to ohmic diffusion can be estimated by dimensional analysis,

$$\tau_d = \frac{\sigma L^2}{c^2}, \tag{4.7}$$

where σ is the electrical conductivity and L is a characteristic length scale. Inserting $L = R$, the stellar radius ~ 10 km, and a typical conductivity of $\sigma = 10^{23} s^{-1}$ gives a decay time of $\sim 10^6$ yr. This is longer than the age of most observed pulsars, so is not likely to have a considerable effect on the global field. However, ohmic diffusion may be important to magnetic and thermal evolution in neutron star crusts, where the conductivity is orders of magnitude lower. We explore a thermo-resistive instability in the crusts of highly magnetized neutron stars in Chapter 5.

5. THERMO-RESISTIVE INSTABILITY IN MAGNETAR CRUSTS

5.1. Introduction

Soft gamma repeaters (SGRs) are a class of highly magnetized neutron stars (magnetars) that exhibit persistent X-ray emission, interrupted periodically by short bursts of gamma rays. The more frequently occurring short bursts have typical durations of 0.01 - 1s, with peak luminosities of $\sim 10^{42}\,\mathrm{erg\,s^{-1}}$. Giant flares are much more rare and energetic outbursts, with peak luminosites $10^2 - 10^5$ times larger than the short bursts. Three giant flares have been observed to date: from SGR 0526-66 on March 5, 1979 (Helfand & Long 1979; Mazets et al. 1979), SGR 1900+14 on August 27, 1998 (Hurley et al. 1999), and SGR 1806-20 on December 27, 2004 (Hurley et al. 2005). SGR 1806-20 has produced the largest observed giant flare, releasing $\sim 10^{46}$ erg of energy over 380 s. Precursors to two of the three giant flares have been identified. The 2004 giant flare was preceded by a 1s long event, 140 s prior to the initial hard spike (Hurley et al. 2005) . A similar precursor to the August 27 giant flare was observed (Ibrahim et al. 2001), with duration $\sim .05\,\mathrm{s}$ preceding the initial spike by 0.4 s.

SGR flares are thought to represent the release of magnetic energy, though the trigger mechanism remains uncertain. Thompson & Duncan (1995) propose that the short bursts observed from SGRs are the result of fracturing the crust of the neutron star by magnetic stresses. Recent calculations indicate that neutron star

crusts fail catastrophically under stress (Horowitz & Kadau 2009). The rigid crust could act as a gate, releasing magnetic energy when magnetic stresses cause the crust to fail. Larger events such as giant flares could be caused by large scale readjustment of the magnetic field due to magnetic instability (Thompson & Duncan 1995). As the field readjusts, magnetic reconnection leads to the formation of a pair plasma which is injected into the magnetosphere (Thompson & Duncan 1995). Alternatively, Lyutikov (2006) argued that the short rise time of the 2004 giant flare requires that the magnetic energy be stored in the magnetosphere rather than the stellar interior. In this scenario, slow untwisting of the internal magnetic field eventually leads to sudden relaxation of the twist in the magnetospheric field, releasing the energy necessary to power the flare.

The initial configuration and subsequent evolution of magnetic fields in highly-magnetized neutron stars is a complicated problem. The field evolves continuously due to the effects of ohmic decay, ambipolar diffusion, and Hall drift. Recently, Pons & Geppert (2007) studied the evolution of magnetic fields in neutron star crusts, emphasizing the importance of Hall drift. Their results indicate that Hall drift of crustal fields can create small-scale magnetic field structures, and that those structures can drift to regions of higher resistivity. The simulations of Pons & Geppert (2007) were restricted to magnetic fields in the inner crust.

In this chapter, we focus on the outer crust, and show that large currents can lead to a thermo-resistive instability, affecting the thermal evolution of the star. As the

instability evolves, large portions of the crust may melt, allowing the magnetic field to evolve on a timescale much faster than the average ohmic decay and Hall timescales. The enhanced magnetic evolution resulting from instability may be related to flare activity in magnetars.

This chapter is organized as follows. In Section 5.2, we describe the relevant physics of the thermo-resistive instability in neutron star crusts. We describe the physical processes that lead to evolution of the neutron star magnetic field in Section 5.3. In Section 5.4, we describe our neutron star model and give details of calculations of the instability growth rate. Section 5.5 contains discussion and our conclusions. Material in this chapter was published in the Monthly Notices of the Royal Astronomical Society (Price et al. 2012).

5.2. Thermo-Resistive Instability

The dipole fields of magnetars are inferred to be in the range $\sim (0.5 - 20) \times 10^{14}$ G, based on spindown measurements of SGRs and AXPs (see Mereghetti 2008 for a review). In order for the magnetic field to be stable in neutron stars, it must contain both toroidal and poloidal components (Markey & Tayler 1973). The toroidal component in a stable configuration may be an order of magnitude larger than the poloidal component (Braithwaite 2009).

Large crustal currents associated with the toroidal field would produce significant ohmic heating due to the relatively high resistivity in the outer crust. Ohmic heating

can account for the observed trend of surface temperature that increases with surface field observed in neutron stars with $B > 10^{13}$ G (Pons et al. 2007). Cooling simulations show that a heating layer in the outer crust, as would arise from current decay, can explain the high surface temperatures of magnetars (Kaminker et al. 2006).

Current decay is determined primarily by electron-phonon interactions for a temperature T below the melting temperature $T_{\rm melt}$. In this regime, the electrical resistivity scales as T, so that a small increase in temperature leads to increased heat dissipation (Figure 35). The additional heating raises the temperature further, and a temperature runaway may develop if thermal transport is unable to quench the feedback process. As we will show in this chapter, this instability can occur in the outer crusts of neutron stars, where the electrical resistivity is relatively high and the thermal conductivity is low.

5.3. Ohmic Decay and Hall Drift

The evolution of the magnetic field in neutron stars after birth is determined primarily by ohmic decay and Hall drift. The ohmic decay timescale is $\tau_{\rm ohm} = \eta^{-1} L^2$, where L is the typical magnetic field length scale and η is the electrical resistivity. A typical value for the outer crust at temperature $T = 10^8$ K is

$$\tau_{ohm} = 3 \times 10^5 \left(\frac{L}{1\,\mathrm{km}} \right)^2 \left(\frac{\eta}{10^{-3}\,\mathrm{cm^2\,s^{-1}}} \right)^{-1} \mathrm{yr}. \tag{5.1}$$

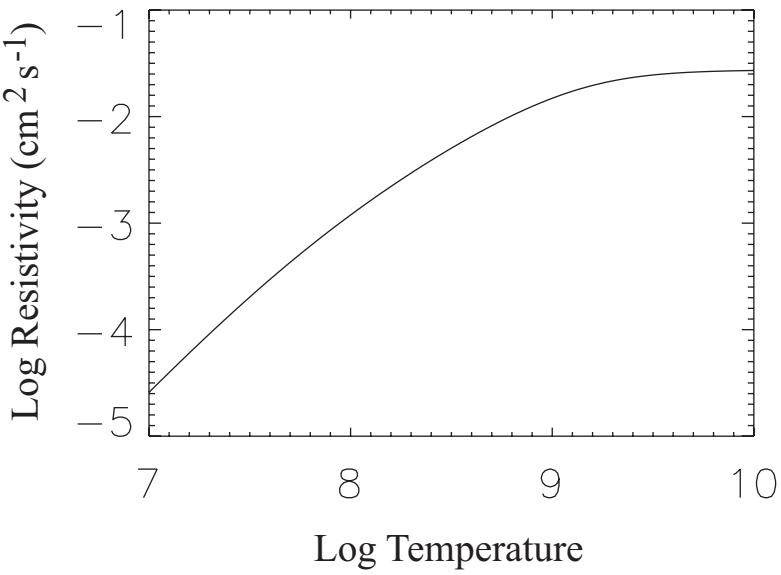

Figure 35. Resistivity of the crust at a density of $10^9\,\mathrm{g\,cm^{-3}}$. The melting temperature at this density is $\sim 3 \times 10^8\,K$.

For a magnetar of age 10^4 yr, crustal currents from the initial field should still be present. (We note that the $\tau_{\rm ohm}$ was smaller early in the star's life, since the temperature and resisitivity were higher.)

Hall drift creates small scale magnetic structures in the crust over the Hall timescale (Pons & Geppert 2007), given by

$$\tau_{Hall} = \frac{4\pi n_e e L^2}{cB}, \tag{5.2}$$

where n_e is the electron density and B is the magnetic field strength. A typical value for the outer crust is

$$\tau_{Hall} \sim 6 \left(\frac{L}{1\,\mathrm{km}}\right)^2 \left(\frac{B}{10^{15}\,G}\right)^{-1} \mathrm{yr}, \tag{5.3}$$

Hall drift can concentrate currents in the crust. The induction equation, neglecting ohmic dissipation, is

$$\frac{\partial \mathbf{B}}{\partial t} = -\nabla \times \left(\frac{c}{4\pi n_e e} (\nabla \times \mathbf{B}) \times \mathbf{B} \right). \tag{5.4}$$

As a simple example to illustrate how Hall drift may affect the magnetic field, consider a field in cylindrical coordinates, with only an azimuthal component which depends on r,

$$\mathbf{B} = B_\phi(r)\hat{\varphi}. \tag{5.5}$$

Eq. (5.4) becomes

$$\frac{\partial \mathbf{B}}{\partial t} = \nabla \times \left(\frac{c}{4\pi n_e e} \frac{B_\phi}{r} \frac{\partial (r B_\phi)}{\partial r} \hat{\mathbf{r}} \right). \tag{5.6}$$

Since the magnetic field has only r dependence, and the quantity inside the parenthesis is in the $\hat{r}$ direction, the curl is zero, and the field is stationary.

Outward drift of the field can replenish currents in the outer crust that are decaying through ohmic diffusion. In order to get an outward drift of the field, the field must have z-dependence, as considered by (Pons & Geppert 2007). This corresponds to a field strength that varies from the magnetic pole to the magnetic equator. The induction equation for the ϕ-component of the field gives

$$\frac{\partial B_\phi}{\partial t} = \frac{2}{\tau_{\rm Hall}} \frac{L^2}{r} \frac{\partial B_\phi}{\partial z}. \tag{5.7}$$

If $\partial B/\partial z$ is positive, the field in the crust will increase over a typical timescale of τ_{Hall}.

We assume henceforth that strong currents exist in the crust at an age of $\sim 10^4$ years, and explore the consequences.

5.4. Calculations

5.4.1. Equations and Boundary Conditions

We model the outer crust as an infinite slab, with $\hat{\mathbf{x}}$ pointing into the star (Figure 36). The thermal evolution of the neutron star outer crust is described by the energy conservation equation,

$$c_v(\rho,T)\frac{dT(x)}{dt} = \frac{4\pi\eta(\rho,T)}{c^2}j^2 + \nabla\cdot[\kappa(\rho,T)\,\nabla T(x)] - Q_\nu(\rho,T), \tag{5.8}$$

where ρ is the density, c_v is the specific heat, $\mathbf{j}$ is the electric current, Q_ν is the neutrino emissivity, and κ is the thermal conductivity. The magnetic field evolution is described by the induction equation

$$\frac{\partial\mathbf{B}(x)}{\partial t} = -\nabla\times(\eta(\rho,T)\nabla\times\mathbf{B}(x))\,, \tag{5.9}$$

where the magnetic field is related to the current by

$$\mathbf{j}(x) = \frac{c}{4\pi}\nabla\times\mathbf{B}(x). \tag{5.10}$$

As justified below, we work in an approximation in which magnetic induction can be ignored, so we need not specify boundary conditions on $\mathbf{B}$. The slab consists of 3 regions - an atmosphere with no magnetic dissipation, an outer crust, and an isothermal inner crust/core. The atmosphere extends from a density of $10^4\,\mathrm{g\,cm^{-3}}$ at the

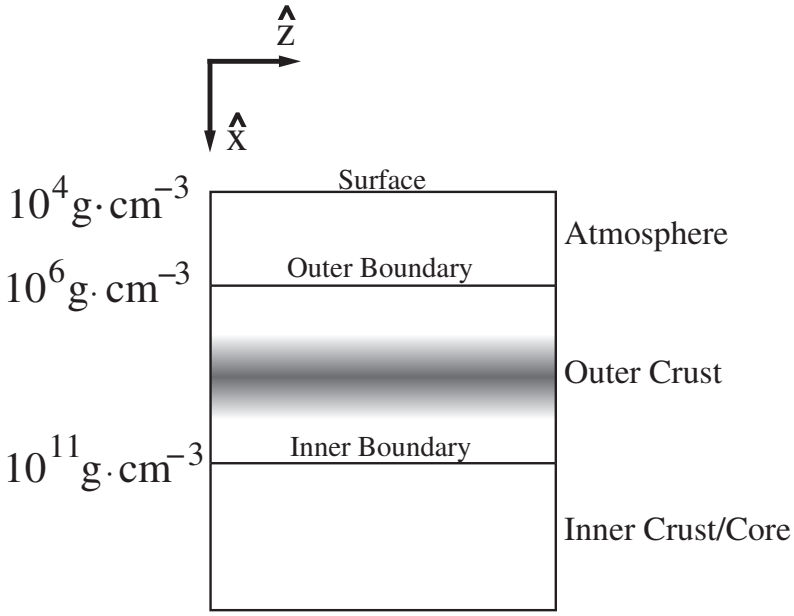

Figure 36. Neutron Star model. The shading represents the region of ohmic heating.

stellar surface to $10^6\,\mathrm{g\,cm^{-3}}$, the outer boundary of the crust. For the atmosphere and outer crust zones, we employ the density model of Friedman & Pandharipande (1981). The inner crust/core zone is assumed to be an infinite heat reservoir, beginning at a density of $\rho = 10^{11}\,\mathrm{g\,cm^{-3}}$.

Boundary conditions. At the stellar surface we choose the unperturbed temperature to be,

$$T = T_s, \tag{5.11}$$

and require that the heat flux at the boundary equal the blackbody emission rate at temperature T_s,

$$\kappa \frac{dT_s}{dx} = \sigma T_s^4. \tag{5.12}$$

As a simple model of the toroidal component of the neutron star magnetic field, we introduce to the outer crust zone a current sheet of width L:

$$\mathbf{j}(x) = j_0 \, e^{-((x-x_0)/2L)^4} \hat{\mathbf{z}}, \tag{5.13}$$

where j_0 is the amplitude of the current, and x_0 the location of the peak current. This analytic form allows a large, nearly uniform current near the heating peak, falling off sharply for $|x - x_0| > L$ (Figure 37). The magnetic field resulting from the current lies in the y-z plane, with variation in the $\hat{\mathbf{x}}$ direction. In our models, the heating region is near the center of the outer crust, with characteristic width much smaller than the crust thickness to ensure negligible heating at the boundaries. We note that this current model leads to large pressure gradients in the crust. To form a stable current model, a complex geometry is required, such as that of Braithwaite (2009). We use the simplified current model described here to demonstrate the thermo-resistive instability.

5.4.2. Input Physics

For the electrical and thermal conductivities in the crust, we use the analytical expressions of Potekhin (1999) for electron-ion collision frequencies in Fe matter. We ignore the effects of the magnetic field on the conductivities. Small jumps in the conductivities occur at $T = T_{melt}$, which we smooth to avoid numerical problems. The heat capacity of the crust has contributions from ions and relativistic electrons. The specific heat due to ions for solid matter ($\gamma > 150$) is given by van Riper (1991),

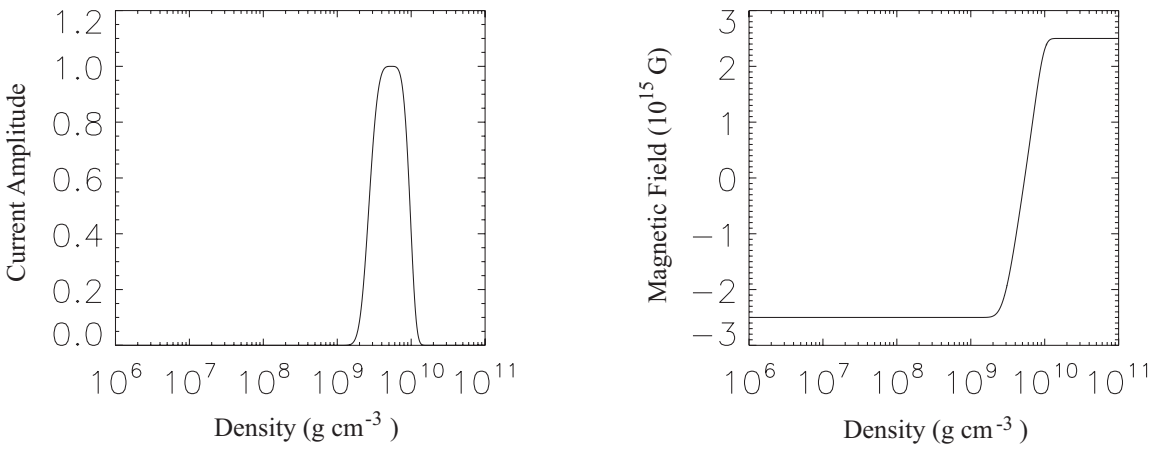

Figure 37. Sample current sheet and associated magnetic field. The current peaks at $x_0 = 100\,\mathrm{m}$,approximately at the center of the outer crust.

$$c_v^{ion} = n_i \frac{3}{2} k_b \left[1 + \frac{\log(\gamma)}{\log(150)}\right] \ \mathrm{erg\,cm^{-3}\,K^{-1}}, \tag{5.14}$$

where

$$\gamma \approx \frac{22.75 Z^2}{T_6} \left(\frac{\rho_6}{A}\right)^{1/3} \tag{5.15}$$

is the Coulomb plasma parameter, ρ_6 is the density in units of $10^6 \mathrm{g\,cm^{-3}}$, T_6 is the temperature in units of 10^6 K, Z is the ionic charge, and A the atomic weight. The contribution from relativistic, degenerate electrons to the specific heat is

$$c_v^e = 5.4 \times 10^{19} \left(\frac{n_e}{n_0}\right)^{2/3} T_9 \ \mathrm{erg\,cm^{-3}\,K^{-1}}, \tag{5.16}$$

where $n_0 = 0.16\,\mathrm{fm^{-3}}$ is the nuclear saturation density. The specific heat of ions and electrons are shown in Figure 38 at 10^8 K.

In strongly-magnetized neutron star crusts, the neutrino luminosity is dominated by neutrino synchroton emission (Aguilera et al. 2008). The rate of emission is given

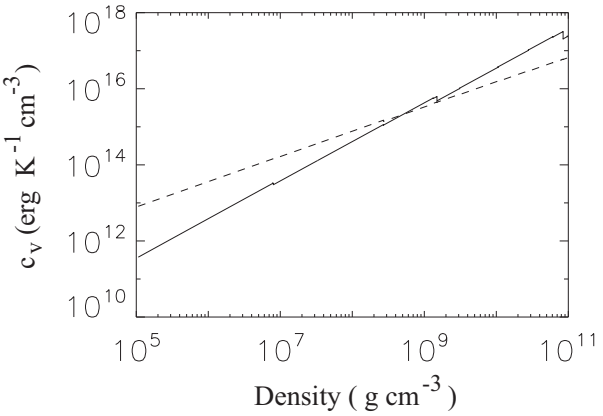

Figure 38. The specific heat at 10^8K. The solid line is ionic specific heat, and the dashed line is electronic specific heat.

by Bezchastnov et al. (1997)

$$Q_\nu = 10^{19} B_{15}^2 T_9^5 \ \mathrm{erg\,cm^{-3}\,s^{-1}}, \tag{5.17}$$

where B_{15} is the magnetic field strength in units of 10^{15} G, and T_9 is the temperature in units of 10^9 K. The ratio of neutrino emission Q_ν to ohmic heating H is given by

$$\frac{Q_\nu}{H} = 7 \times 10^{-5}\, B_{15}^2\, T_8^5 \left(\frac{\eta}{10^{-4}\,\mathrm{cm\,s}}\right)^{-1} \left(\frac{j}{10^{21}\,(\mathrm{erg\,cm^{-3}\,s^{-2}})^{1/2}}\right)^{-2}. \tag{5.18}$$

For the range of temperatures and magnetic fields we consider, the energy lost through neutrino emission is negligible compared to the ohmic heating rate and we neglect it in this analysis.

Using these boundary conditions, we integrate Eq.(5.8) to the boundary of the outer crust. An example of a typical equilibrium crust temperature profile is plotted in Figure 39, corresponding to the current model shown in Figure 37. The heat current for a typical crust model is shown in Figure 40. Most of the energy flux is

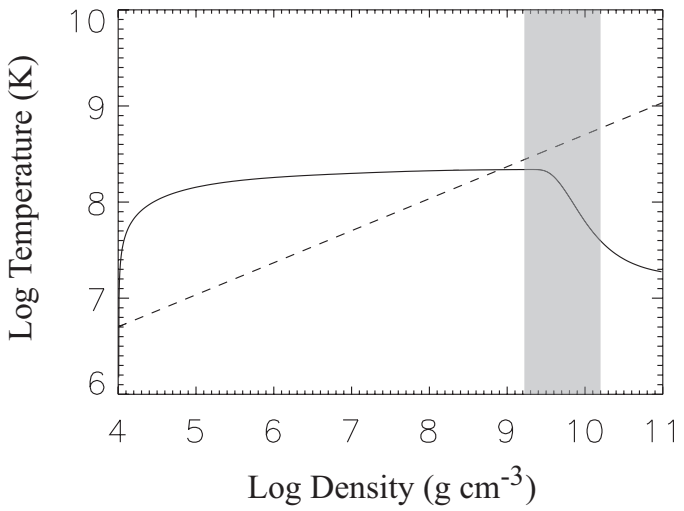

Figure 39. A sample temperature profile, with $T_s = 10^6$ K, $B_{max} = 5 \times 10^{15}$ G. The dashed curve is the melting temperature of the lattice. Shading indicates the heated region. This model indicates that a portion of the crust is molten, but the heated region is solid.

into the star, in the direction of increasing thermal conductivity. The energy is then lost to neutrino emission from the core.

5.4.3. Stability Analysis

We now examine the stability of the equilibrium state . We perform a stability analysis of the outer crust using Eq. (5.8), substituting $T(t) = T_0 + \delta T e^{\gamma t}$, where δT is the perturbation mode and γ is the growth (decay) rate. For the range of heating models we consider, instability growth rates are fast compared to magnetic diffusion and we neglect evolution of the magnetic field in our calculations. The following section contains further justification of this approximation. Neglecting magnetic evolution and neutrino emission, the perturbed energy balance equation is given by

$$\frac{\partial^2 \delta T}{\partial x^2} = \frac{1}{\kappa}\left[c_v \gamma - \frac{4\pi}{c^2}\eta' j_0^2 - \frac{\partial \kappa'}{\partial x}\frac{\partial T_0}{\partial x} - \kappa' \frac{\partial^2 T_0}{\partial x^2}\right]\delta T - \frac{1}{\kappa}\left[\frac{\partial \kappa_0}{\partial x} + \kappa' \frac{\partial T_0}{\partial x}\right]\frac{\partial \delta T}{\partial x}, \quad (5.19)$$

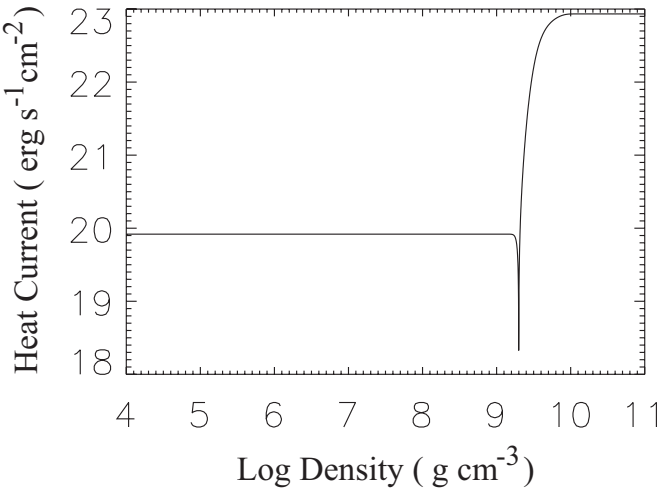

Figure 40. Absolute value of the heat current for a sample crust model. The heat current flows towards the surface and the core from the heating peak. Most of the flux is lost to the core .

where primes indicate differentiation with respect to T at fixed x.

5.4.4. Magnetic Induction

To determine the relevance of magnetic induction to the instability growth rate we perform a local, plane-wave analysis of Eqs. (5.19) and (5.9). The perturbed energy conservation equation including magnetic induction is given by

$$\kappa\frac{\partial^2\delta T}{\partial x^2} = \left[c_v\gamma - \frac{4\pi}{c^2}\eta' j_0^2 - \frac{\partial\kappa'}{\partial x}\frac{\partial T_0}{\partial x} - \kappa'\frac{\partial^2 T_0}{\partial x^2}\right]\delta T - \left[\frac{\partial\kappa_0}{\partial x} + \kappa'\frac{\partial T_0}{\partial x}\right]\frac{\partial\delta T}{\partial x} - \left[\frac{8\pi}{c^2}\,\eta\, j_0\right]\delta j. \tag{5.20}$$

The magnetic induction equation (Eq. 5.9) can be written in terms of the current $\mathbf{j}$,

$$\frac{\partial\mathbf{j}}{\partial t} = -\nabla\times(\nabla\times\eta\mathbf{j}). \tag{5.21}$$

Upon linearizing the induction equation, we have

$$\begin{aligned}\eta_0 \frac{\partial^2 \delta j}{\partial x^2} &= \left[\gamma - \frac{\partial^2 \eta_0}{\partial x^2}\right] \delta j - 2\frac{\partial \eta_0}{\partial x}\frac{\partial \delta j}{\partial x} - \left[2\frac{\partial \eta'}{\partial x}\frac{\partial j_0}{\partial x} + \eta' \frac{\partial^2 j_0}{\partial x^2} + \frac{\partial^2 \eta'}{\partial x^2} j_0\right] \delta T \\ &\quad - \left[2\frac{\partial \eta'}{\partial x} j_0 + 2\eta' \frac{\partial j}{\partial x}\right] \frac{\partial \delta T}{\partial x} - \eta' j_0 \frac{\partial^2 \delta T}{\partial x^2}. \end{aligned} \tag{5.22}$$

Magnetic induction can be neglected if the induction term is small compared to the ohmic heating term in Eq. (5.20), integrated over the heating region:

$$\int_V \frac{4\pi}{c^2} \eta' j_0^2 \gg \int_V \frac{8\pi}{c^2}\, \eta_0\, j_0\, f(x), \tag{5.23}$$

where $f(x) \equiv \delta j / \delta T$. We find an approximate expression for $f(z)$ using plane wave solutions for δT and δj in Eq. (5.22) and solving for δj:

$$\begin{aligned}\delta j &= \left[k^2 \eta_0 + \gamma - \frac{d^2 \eta_0}{dx^2} - 2ik\frac{\eta_0}{dx}\right]^{-1} \times \\ &\quad \left[2\frac{d\eta'}{dx}\frac{dj_0}{dx} + \eta' \frac{d^2 j_0}{dx^2} + \frac{d^2 \eta'}{dx^2} j_0 + 2ik\frac{d\eta'}{dx} j_0 + 2ik\eta' \frac{dj_0}{dx} - \eta' j_0 k^2\right] \delta T. \end{aligned} \tag{5.24}$$

We take for the wavenumber $k = 1/L$, the characteristic width of the heating region. We approximate the induction term by evaluating the variables at the heating peak,

$$\int_V \frac{8\pi}{c^2}\, \eta_0\, j_0\, f(x) \simeq \frac{8\pi}{c^2}\, L\, \eta_p\, j_{max}\, f(x), \tag{5.25}$$

where L is the heating length scale, η_p is the resistivity at the heating peak, j_{max} is the maximum current, and $f(x)$ is evaluated at the heating peak in the plane wave approximation. We approximate the heating term in the same way,

$$\int_V \frac{4\pi}{c^2}\eta' j_0^2 \simeq \frac{4\pi}{c^2} L_h \eta_p' j_{max}^2, \tag{5.26}$$

where η_p' is $\frac{\partial \eta}{\partial T}$ evaluated at the peak. Using Eqs. (5.25) and (5.26), Eq. (5.23) becomes

$$\frac{4\pi}{c^2} L_h \eta_p' j_{max}^2 \gg \frac{8\pi}{c^2}\, L_h\, \eta_p\, j_{max}\, f(x). \tag{5.27}$$

For the range of magnetic field models we consider, the heating term is much larger than the induction term. We plot the ratio of the heating term to induction term in Fig. 41 for several models. We conclude that magnetic induction is negligible for the large fields of interest.

As a second test, we evaluate the ohmic decay time of the magnetic field by dimensional analysis. Dimensionally, the ohmic decay time is

$$\tau_d \sim \frac{L^2}{4\pi\eta}, \tag{5.28}$$

where η is the resistivity at the heating peak, and L is a characteristic length scale. Ohmic diffusion can be neglected if the ohmic decay timescale is much longer than the instability growth timescale, $\tau_d \gg \tau_g$. Fig. 42 shows the ratio τ_d/τ_g for several heating models.

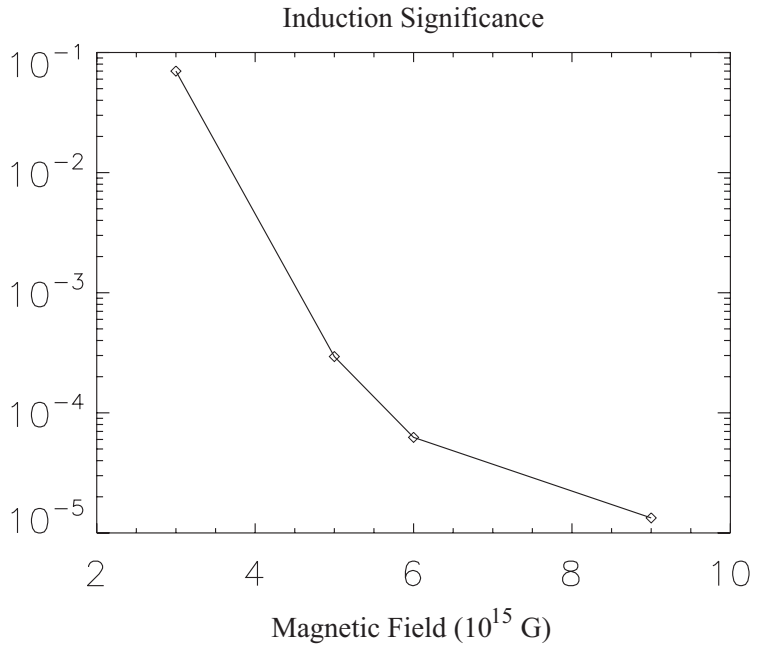

Figure 41. Ratio of induction term to heating term in the energy balance equation. Induction can be neglected for small values of this ratio .

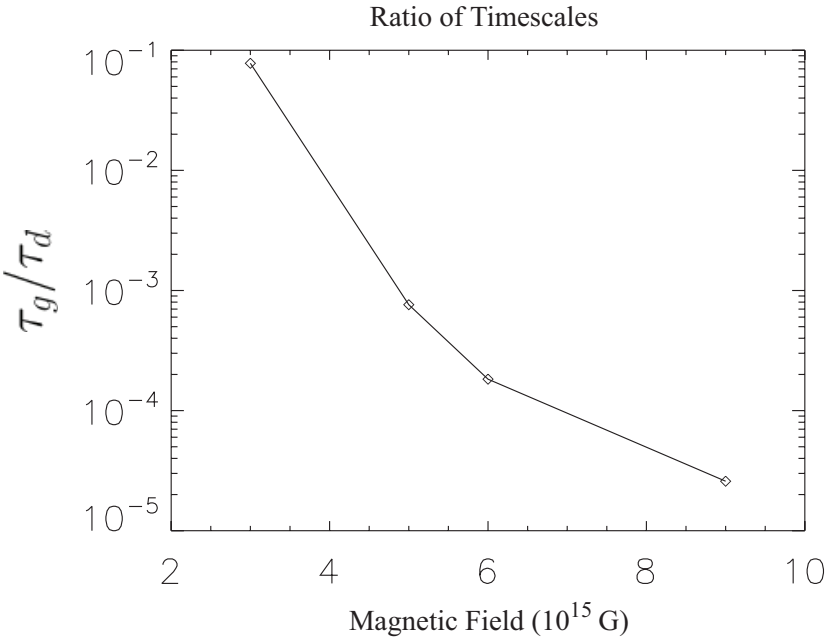

Figure 42. Ratio of instability growth timescale to ohmic decay timescale for several heating models. Magnetic induction can be neglected for $\tau_g/\tau_d \ll 1$.

5.4.5. Perturbation Mode Boundary Conditions.

To determine the perturbation mode gradient at the outer boundary, ($\rho = 10^6 g\, cm^{-3}$), we integrate through the atmosphere for several values of T_s to determine the dependence of the temperature gradient on the temperature. Because there is no ohmic heating in the atmosphere section, the temperature at the outer boundary T_{ob} and the temperature gradient dT_{ob}/dx are uniquely defined for a given surface temperature. Therefore, dT_{ob}/dx is a function of T_{ob}:

$$\frac{dT_{ob}}{dx} = f(T_{ob}) \tag{5.29}$$

Allowing perturbations to the temperature at the outer boundary for Eq. (5.29) gives

$$\frac{d(T_{ob} + \delta T_{ob})}{dx} = f(T_{ob} + \delta T_{ob}). \tag{5.30}$$

Since the function $f(T_{ob})$ is well behaved, Eq. (5.30) to first order in δT_{ob} is

$$\frac{d(T_{ob} + \delta T_{ob})}{dx} = f(T_{ob}) + f'(T_{ob})\delta T_{ob}, \tag{5.31}$$

where primes indicate differentiation with respect to T_{ob}. Using Eq. (5.29) we can solve for $f'(T_{ob})$,

$$f'(T_{ob}) = \frac{d}{dT_{ob}}\left(\frac{dT_{ob}}{dx}\right). \tag{5.32}$$

Keeping only perturbed terms of Eq. (5.32) we arrive at the outer boundary condition,

$$\frac{d\delta T_{ob}}{dx} = \frac{d}{dT_{ob}}\left(\frac{dT_{ob}}{dx}\right)\delta T_{ob}. \tag{5.33}$$

We assume the inner crust/core of the neutron star to be an infinite heat reservoir. Therefore, at the inner boundary we require that the temperature perturbation vanish,

$$\delta T_{ib} = 0. \tag{5.34}$$

We solve Eq. (5.19) simultaneously for the temperature perturbation mode $\delta T(x)$ and the mode growth rate γ for a given crust temperature profile and current distribution, given by Eq. (5.13). We satisfy the set of mixed boundary conditions through a shooting algorithm. A sample temperature perturbation mode for the heating model presented previously is plotted in Figure 43. The instability growth rate γ as a function of the maximum field in the crust due to crustal currents is plotted in Figure 44.

To see the scalings of γ with the parameters of the problem, it is useful to perform a local plane wave analysis to obtain an approximate analytical expression. Solving Eq. (5.19), assuming that κ has only weak dependence on T and x and keeping only the dominant terms (determined by numerical experiment), we obtain

$$\frac{\partial^2 \delta T}{\partial x^2} = \frac{1}{\kappa}\left[c_v\gamma - \frac{4\pi}{c^2}\eta' j_0^2\right]\delta T. \tag{5.35}$$

Substituting plane-wave solutions for δT with $k = 1/L$ gives an approximate expression for the mode growth rate,

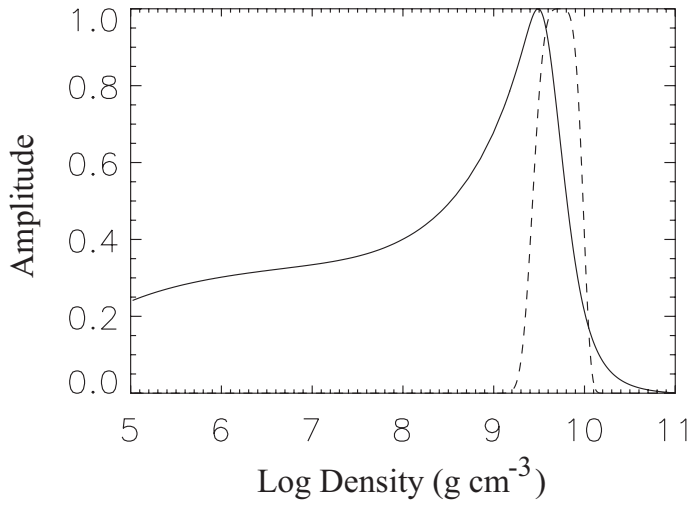

Figure 43. Sample unstable temperature perturbation mode, corresponding to the same crust model as Fig. 6. Dashed curve indicates the (normalized) electric current amplitude. Units are arbitrary.

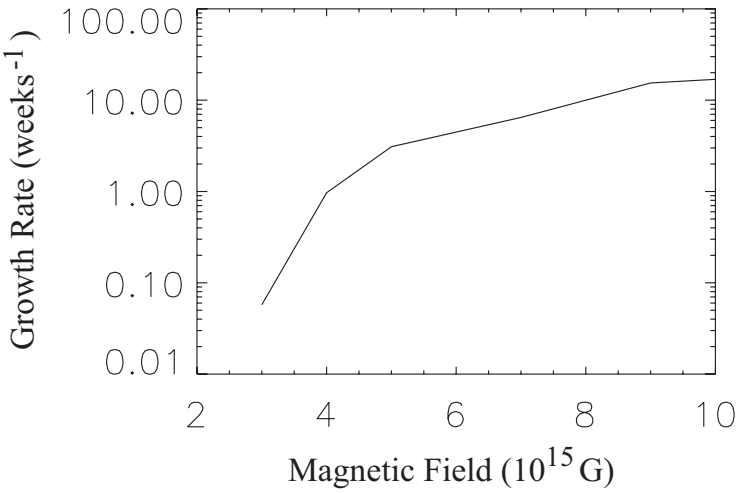

Figure 44. Instability growth rate γ vs maximum field in the crust, for heating peaked at $\rho = 3 \times 10^9 \mathrm{g\,cm^{-3}}$. The minimum field required for instability is $B = 3 \times 10^{15}$ G.

$$\gamma \sim \frac{1}{c_v}\left[\frac{4\pi}{c^2}\eta_p' j_p^2 - \frac{\kappa_p}{L^2}\right], \tag{5.36}$$

where all parameters are evaluated at the heating peak. Eq. (5.36) shows the competition between the ohmic heating (the first term), and cooling through thermal diffusion (the second term). Changing the surface temperature affects the growth rate by changing the crust temperature at the heating location. If the crust temperature is much greater than T_{melt}, the temperature sensitivity of the resistivity η becomes negligible and the heating feedback effect is lost, thereby stabilizing the system. Increasing the current amplitude gives more thermal energy to drive the instability. The growth rate is somewhat insensitive to the choice of L. However, the relationship between the magnetic field and the current (Equation 5.10) indicates that for a fixed magnetic field, j_0 varies inversely with L. To obtain crust models with realistic magnetic field amplitudes, the electric current must be concentrated in a relatively small region of the crust. Finally, the instability growth rate is highly dependent on the heating location x_0 due to the spatial variation of both the thermal conductivity and the electrical resistivity. A fixed current will produce the most heat in regions of high resistivity. Heat produced in regions of low thermal conductivity is most likely to lead to instability, as the heat is not efficiently carried away. For these reasons, heating near the surface of the star is most unstable.

We calculate the instability growth rate for a wide range of heating models - characteristic heating widths range from $5\,\mathrm{m} < \mathrm{L} < 50\,\mathrm{m}$, and heating peak locations

$10^8\,\mathrm{g\,cm^{-3}} < \rho_0 < 10^{10}\,\mathrm{g\,cm^{-3}}$. In this range, the current amplitude is virtually zero at the inner and outer boundaries. We consider current amplitudes corresponding to maximum magnetic fields from 10^{15} G to 10^{16} G. The steady state surface temperature T_s is not the same for each heating model. We calculate crust temperature profiles with 10^6 K $< T_s < 10^7$ K, seeking models for which the temperature in the heating region is less than or equal to the melting temperature, and the temperature at the inner boundary is 10^7 K $< T_{ib} < 10^8$ K. Maintaining a crust temperature below T_{melt} ensures that the resistivity feedback is operating at the heating location, and 10^7 K $< T_{ib} < 10^8$ K ensures that the core temperature is in the appropriate range for a magnetar with a characteristic age of 10^4 yr (Aguilera et al. 2008) . These conditions lead to a narrow range of values for the surface temperature. Fig. 45 illustrates the region of instability for given values of the maximum field, B_{max}, and the core temperature of the neutron star for fixed heating width and location. Subject to the conditions mentioned above, our results show that a minimum crustal field of $B = 3\times10^{15}$ G is required to destabilize the crust. Instability growth rates for several models are plotted in Fig. 46. To find an approximate expression for the critical field required to give instability ($\gamma > 0$), we substitute $j \sim cB_0/4\pi L$ in Eq. (5.36) and solve for the critical field,

$$B_{\rm crit} = 2.5\times10^{15}\left(\frac{\kappa}{2\times10^{18}\,\mathrm{erg\,s^{-1}\,cm^{-1}\,K^{-1}}}\right)\left(\frac{\eta'}{4\times10^{-12}\,\mathrm{cm^2\,s^{-1}}}\right)^{-1}\ \mathrm{G}. \quad (5.37)$$

This estimate agrees well with our numerical solutions.

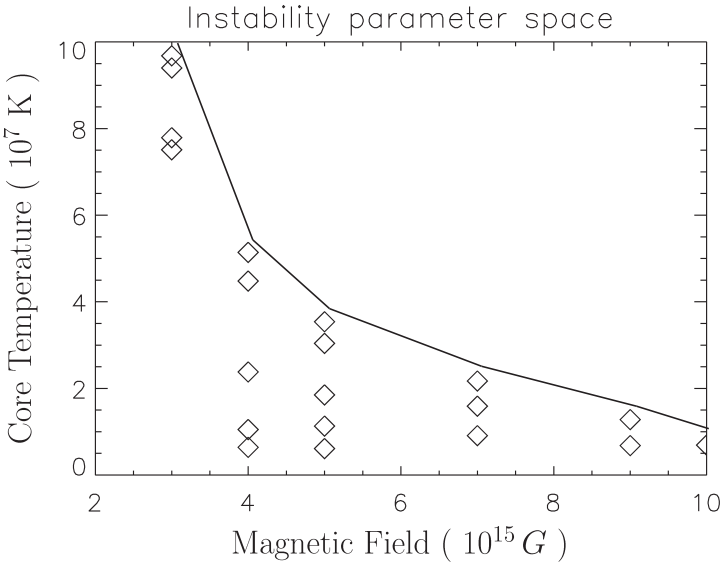

Figure 45. Diamonds represent values of the crust magnetic field and the neutron star core temperature for which unstable modes are found. The solid line indicates the approximate boundary between unstable and stable parameter space. All models use a heating width of 20 m, with heating location $\rho_0 = 3 \times 10^9 \mathrm{gcm}^{-3}$.

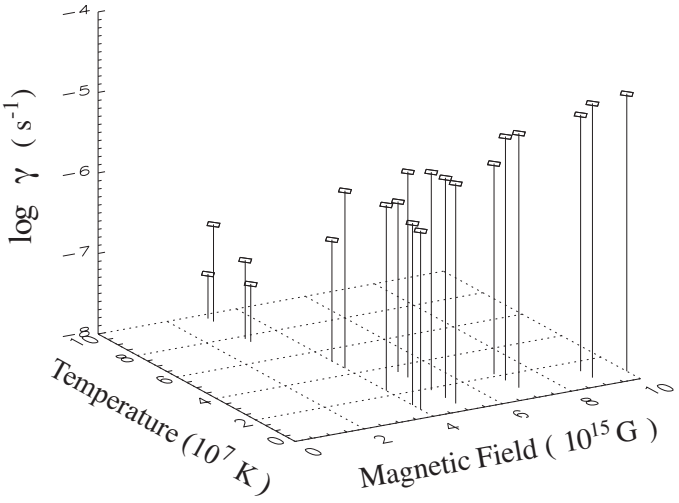

Figure 46. The instability growth rate as a function of the neutron star core temperature and the crust magnetic field. All models used a heating width of 20 m, with heating location $\rho_0 = 3 \times 10^9 \mathrm{gcm}^{-3}$.

5.5. Discussion and Conclusions

Large crustal currents associated with the magnetic field of magnetars may lead to a thermo-resistive instability in the crust. Calculations of the instability growth time for a model neutron star crust give typical growth times of weeks to months. These timescales are short compared to the ohmic diffusion timescale of the magnetic field.

We conclude that the instability identified in this chapter may operate in neutron star crusts for a wide range of physical parameters relevant to magnetars. Heating may be located anywhere in the outer crust, while magnetic length scales need only be comparable to the crust thickness or smaller. Instability occurs for crust temperatures $T_{\rm crust} \sim 5 \times 10^8$ K or lower, characteristic of relatively young magnetars, $\tau_{\rm age} \sim 10^4$ yrs (Aguilera et al. 2008) . This result coincides with the inferred age of magnetar candidates associated with supernova remnants (see Mereghetti (2008) for a review) . Additionally, we find that only heating models that produce large magnetic fields ($B > 10^{15}$ G) will produce instability, so this instability is specific to magnetars. The characteristic temperatures and magnetic fields at which the thermo-resistive instability occurs suggest an intriguing connection between this instability and magnetars. We note that our simplified treatment of the current sheet is likely to overestimate the critical field required for instability by a factor of order unity. A stable current sheet necessarily has a more complicated structure than assumed here. The components of the current that we have neglected will lead to further heating.

Model	B (G)	$\dot{Q}(\mathrm{ergs}^{-1})$	E_B (erg)
1	10^{15}	2×10^{35}	5.7×10^{45}
2	5×10^{15}	10^{36}	1.4×10^{47}
3	10^{16}	2×10^{36}	5.6×10^{47}

Table 3. Magnetic field, heat deposition rate and magnetic energy in the crust for 3 heating models..

While we restrict our models to heating in the outer crust, instability in the inner crust could arise in the same way. Heat and charge transport mechanisms are no different, and we expect the scaling of Eq. (5.36) for the growth rate to apply to inner crust heating. However, because of the larger thermal conductivity in the inner crust, deeper crustal currents would have to be larger to produce similar instability growth rates to those calculated here. As the heating is moved to deeper layers, the minimum magnetic field required for instability becomes greater than 10^{16} G.

The magnetic energy in the crust for our higher heating models is sufficient to power even the largest giant flares. The magnetic energy contained in the magnetic field in the crust is given by

$$E_B = 4\pi \int r^2 \frac{B(r)^2}{8\pi}\, dr, \tag{5.38}$$

where we integrate from the inner boundary to the stellar surface. We calculate the maximum field in the crust, the rate of energy deposition due to crustal currents, and the magnetic energy in the outer crust for several heating models (Table 3). The energy released during the largest giant flare to date was approximately 10^{46} erg.

Future work is required to determine the nonlinear evolution of the magnetic field once an instability is triggered. Solving the coupled energy conservation and magnetic induction equations as a function of time will give insight into this problem. Our solutions for the steady state temperature indicate that a portion of the crust is molten. As the instability grows, higher density regions of the crust may melt, reducing the maximum magnetic stress that could be supported by the crust. Simulations of the magneto-thermal evolution could provide a link between the instability we have identified and glitch behavior in magnetars.

REFERENCES CITED

[1] Aguilera, D. N., Pons, J. A., and Miralles, J. A. 2D Cooling of magnetized neutron stars. *A&A 486* (July 2008), 255–271.

[2] Alpar, M. A., Anderson, P. W., Pines, D., and Shaham, J. *Astrophys. J. 276* (1984), 325.

[3] Anderson, P. W., and Itoh, N. Pulsar glitches and restlessness as a hard superfluidity phenomenon. *Nature 256* (July 1975), 25–27.

[4] Avogadro, P., Barranco, F., Broglia, R. A., and Vigezzi, E. Vortex nucleus interaction in the inner crust of neutron stars. *Nuclear Physics A 811* (Oct. 2008), 378–412.

[5] Baym, G., Pethick, C., and Sutherland, P. The Ground State of Matter at High Densities: Equation of State and Stellar Models. *Astrophys. J. 170* (Dec. 1971), 299.

[6] Bezchastnov, V. G., Haensel, P., Kaminker, A. D., and Yakovlev, D. G. Neutrino synchrotron emission from dense magnetized electron gas of neutron stars. *A&A 328* (Dec. 1997), 409–418.

[7] Bhattacharya, D., and van den Heuvel, E. P. J. Formation and evolution of binary and millisecond radio pulsars. *Phys. Rep. 203* (1991), 1–124.

[8] Bildsten, L. Thermonuclear Burning on Rapidly Accreting Neutron Stars. In *NATO ASIC Proc. 515: The Many Faces of Neutron Stars.* (1998), R. Buccheri, J. van Paradijs, & A. Alpar, Ed., p. 419.

[9] Boynton, P. E. In *IAU Symposium No. 95, Pulsars* (Dordrecht, 1981), R. Wielebinski and W. Sieber, Eds., Reidel, p. 279.

[10] Boynton, P. E., and Deeter, J. E. In *Compact Galactic X-ray Sources* (Urbana, 1979), F. K. Lamb and D. Pines, Eds., University of Illinois, p. 168.

[11] Boynton, P. E., Deeter, J. E., Lamb, F. K., Zylstra, G., Pravdo, S. H., White, N. E., Wood, K. S., and Yentis, D. J. *Astrophys. J. 283* (1984), L53.

[12] Boynton, P. E., Groth, E. J., Hutchinson, D. P., Jr., G. P. N., Partridge, R. B., and Wilkinson, D. T. Optical Timing of the Crab Pulsar, NP 0532. *Astrophys. J. 175* (July 1972), 217.

[13] Braithwaite, J. Axisymmetric magnetic fields in stars: relative strengths of poloidal and toroidal components. *MNRAS 397* (Aug. 2009), 763–774.

[14] Brecher, K. Her X-1: A Processing Binary Pulsar? *Nature 239* (Oct. 1972), 325–326.

[15] Chamel, N., and Haensel, P. Physics of Neutron Star Crusts. *Living Reviews in Relativity 11* (Dec. 2008), 10.

[16] Cheng, K. S. *Astrophys. J. 321* (1987), 799.

[17] Cheng, K. S. *Astrophys. J. 321* (1987), 805.

[18] Cordes, J. M., and Helfand, D. J. Pulsar timing. III - Timing noise of 50 pulsars. *Astrophys. J. 239* (July 1980), 640–650.

[19] Cordes, J. M., and Shannon, R. M. Rocking the Lighthouse: Circumpulsar Asteroids and Radio Intermittency. *Astrophys. J. 682* (Aug. 2008), 1152–1165.

[20] Dall'Osso, S., Granot, J., and Piran, T. Magnetic field decay in neutron stars: from Soft Gamma Repeaters to "weak field magnetars". *ArXiv e-prints* (Oct. 2011).

[21] Dodson, R. G., McCulloch, P. M., and Lewis, D. R. High Time Resolution Observations of the January 2000 Glitch in the Vela Pulsar. *Astrophs. J. Lett. 564* (Jan. 2002), L85–L88.

[22] Donati, P., and Pizzochero, P. M. Is there Nuclear Pinning of Vortices in Superfluid Pulsars? *Physical Review Letters 90*, 21 (May 2003), 211101.

[23] Edelson, R. A., and Krolik, J. H. *Astrophys. J. 333* (1988), 646.

[24] Espinoza, C. M., Lyne, A. G., Stappers, B. W., and Kramer, M. A study of 315 glitches in the rotation of 102 pulsars. *Mon. Not. R. Astron. Soc. 414* (June 2011), 1679–1704.

[25] Friedman, B., and Pandharipande, V. R. Hot and cold, nuclear and neutron matter. *Nuclear Physics A 361* (May 1981), 502–520.

[26] Gold, T. Rotating Neutron Stars as the Origin of the Pulsating Radio Sources. *Nature 218* (May 1968), 731–732.

[27] Goldreich, P., and Julian, W. H. Pulsar Electrodynamics. *Astrophys. J. 157* (Aug. 1969), 869.

[28] Goldreich, P., and Reisenegger, A. Magnetic field decay in isolated neutron stars. *Astrophys. J. 395* (Aug. 1992), 250–258.

[29] Gudmundsson, E. H., Pethick, C. J., and Epstein, R. I. Neutron star envelopes. *Astrophys. J. Lett. 259* (Aug. 1982), L19–L23.

[30] Guillot, S., Rutledge, R. E., and Brown, E. F. Neutron Star Radius Measurement with the Quiescent Low-mass X-ray Binary U24 in NGC 6397. *Astrophys. J. 732* (May 2011), 88.

[31] Helfand, D. J., and Long, K. S. X-ray observations of the 5 march 1979 gamma-burst field. *Nature 282* (Dec. 1979), 589–591.

[32] Hewish, A., Bell, S. J., Pilkington, J. D. H., Scott, P. F., and Collins, R. A. Observation of a Rapidly Pulsating Radio Source. *Nature 217* (Feb. 1968), 709–713.

[33] Hobbs, G., Lyne, A. G., and Kramer, M. An analysis of timing irregularities for 366 pulsars. *Mon. Not. R. Astron. Soc. 402* (2010), 1027.

[34] Hobbs, G., Lyne, A. G., Kramer, M., Martin, C. E., and Jordan, C. Long-term timing observations of 374 pulsars. *Mon. Not. R. Astron. Soc. 353* (Oct. 2004), 1311–1344.

[35] Hobbs, G., Lyne, A. G., Kramer, M., Martin, C. E., and Jordan, C. Long-term timing observations of 374 pulsars. *Mon. Not. R. Astron. Soc. 353* (Oct. 2004), 1311–1344.

[36] Honnappa, S., Lewandowski, W., Kijak, J., Deshpande, A. A., Gil, J., Maron, O., and Jessner, A. Single pulse analysis of PSR B1133+16 at 8.35 GHz and carousel circulation time. *ArXiv e-prints* (Sept. 2011).

[37] Horowitz, C. J., and Kadau, K. Breaking Strain of Neutron Star Crust and Gravitational Waves. *Physical Review Letters 102*, 19 (May 2009), 191102–+.

[38] Hurley, K., Boggs, S. E., Smith, D. M., Lin, R. C. D. R., Zoglauer, A., Krucker, S., Hurford, G., Hudson, H., Wigger, C., Hajdas,

W., Thompson, C., Mitrofanov, I., Sanin, A., Boynton, W., Fellows, C., von Kienlin, A., Lichti, G., Rau, A., and Cline, T. An exceptionally bright flare from sgr 1806-20 and the origins of short-duration γ-ray bursts. *Nature 434* (Apr. 2005), 1098–1103.

[39] Hurley, K., Cline, T., Mazets, E., Barthelmy, S., Butterworth, P., Marshall, F., Palmer, D., Aptekar, R., Golenetskii, S., Il'Inskii, V., Frederiks, D., McTiernan, J., Gold, R., and Trombka, J. A giant periodic flare from the soft γ-ray repeater SGR1900+14. *Nature 397* (Jan. 1999), 41–43.

[40] Ibrahim, A. I., Strohmayer, T. E., Woods, P. M., Kouveliotou, C., Thompson, C., Duncan, R. C., Dieters, S., Swank, J. H., van Paradijs, J., and Finger, M. An Unusual Burst from Soft Gamma Repeater SGR 1900+14: Comparisons with Giant Flares and Implications for the Magnetar Model. *ApJ 558* (Sept. 2001), 237–252.

[41] Kaminker, A. D., Yakovlev, D. G., Potekhin, A. Y., Shibazaki, N., Shternin, P. S., and Gnedin, O. Y. Magnetars as cooling neutron stars with internal heating. *MNRAS 371* (Sept. 2006), 477–483.

[42] Kaspi, V. M., and Gavriil, F. P. A Second Glitch from the "Anomalous" X-Ray Pulsar 1RXS J170849.0-4000910. *Astrophys. J. Lett. 596* (Oct. 2003), L71–L74.

[43] Lamb, F. K., Pines, D., and Shaham, J. *Astrophys. J. 225* (1978), 582.

[44] Larson, M. B., and Link, B. Simulations of glitches in isolated pulsars. *Mon. Not. R. Astron. Soc. 333* (July 2002), 613–622.

[45] Lattimer, J. M., and Prakash, M. Ultimate Energy Density of Observable Cold Baryonic Matter. *Physical Review Letters 94*, 11 (Mar. 2005), 111101.

[46] Link, B., and Epstein, R. I. Precession Interpretation of the Isolated Pulsar PSR B1828-11. *Astrophys. J. 556* (July 2001), 392–398.

[47] Link, B., Epstein, R. I., and Baym, G. *Astrophys. J. 403* (1993), 285.

[48] Lohsen, E. Third speed-up of the Crab pulsar. *Nature 258* (Dec. 1975), 688.

[49] Lohsen, E. H. G. Optical timing observations of the Crab pulsar 1968-1979. *Astron. Astrophys. Suppl. Ser. 44* (Apr. 1981), 1–14.

[50] Lyne, A., Hobbs, G., Kramer, M., Stairs, I., and Stappers, B. Switched Magnetospheric Regulation of Pulsar Spin-Down. *Science 329* (July 2010), 408–.

[51] Lyne, A. G., and Graham-Smith, F. *Pulsar Astronomy*. Cambridge University Press, July 2005.

[52] Lyne, A. G., Shemar, S. L., and Smith, F. G. *Mon. Not. Roy. Astr. Soc. 315* (2000), 534.

[53] Lyutikov, M. Magnetar giant flares and afterglows as relativistic magnetized explosions. *MNRAS 367* (Apr. 2006), 1594–1602.

[54] Markey, P., and Tayler, R. J. The adiabatic stability of stars containing magneticfields-II. Poloidal fields. *MNRAS 163* (1973), 77–+.

[55] Maxwell, O. V. Neutron star cooling. *Astrophys. J. 231* (July 1979), 201–210.

[56] Mazets, E. P., Golenetskij, S. V., and Guryan, Y. A. Soft gamma-ray bursts from the source B1900+14. *Soviet Astronomy Letters 5* (Dec. 1979), 343–+.

[57] Mereghetti, S. The strongest cosmic magnets: soft gamma-ray repeaters and anomalous X-ray pulsars. *A&AR 15* (July 2008), 225–287.

[58] Migdal, A. Superfluidity and the moments of inertia of nuclei. *Nuc. Phys. 13* (Nov. 1959), 655–674.

[59] Özel, F., Gould, A., and Güver, T. The Mass and Radius of the Neutron Star in the Bulge Low-mass X-Ray Binary KS 1731-260. *Astrophys. J. 748* (Mar. 2012), 5.

[60] Page, D., Lattimer, J. M., Prakash, M., and Steiner, A. W. Minimal Cooling of Neutron Stars: A New Paradigm. *Astrophys. J. Suppl. Ser. 155* (Dec. 2004), 623–650.

[61] Pavlov, G. G., and Zavlin, V. E. Thermal radiation from cooling neutron stars. In *Texas in Tuscany. XXI Symposium on Relativistic Astrophysics* (Sept. 2003), R. Bandiera, R. Maiolino, & F. Mannucci, Ed., pp. 319–328.

[62] Pizzochero, P. M. Angular momentum transfer in vela-like pulsar glitches. *Atrophys. J. L. 743* (2011), L20.

[63] Pons, J. A., and Geppert, U. Magnetic field dissipation in neutron star crusts: from magnetars to isolated neutron stars. *A&A 470* (July 2007), 303–315.

[64] Pons, J. A., Link, B., Miralles, J. A., and Geppert, U. Evidence for Heating of Neutron Stars by Magnetic-Field Decay. *Physical Review Letters 98*, 7 (Feb. 2007), 071101–+.

[65] Potekhin, A. Y. Electron conduction in magnetized neutron star envelopes. *A&A 351* (Nov. 1999), 787–797.

[66] Price, S., Link, B., Epstein, R. I., and Li, H. Thermoresistive instability in magnetar crusts. *Mon. Not. R. Astron. Soc. 420* (Feb. 2012), 949–956.

[67] Ravenhall, D. G., Pethick, C. J., and Wilson, J. R. Structure of Matter below Nuclear Saturation Density. *Physical Review Letters 50* (June 1983), 2066–2069.

[68] Reisenegger, A. Origin and evolution of neutron star magnetic fields. *ArXiv Astrophysics e-prints* (July 2003).

[69] Ruderman, M. Neutron Starquakes and Pulsar Periods. *Nature 223* (Aug. 1969), 597–598.

[70] Sawyer, R. F., and Scalapino, D. J. Pion Condensation in Superdense Nuclear Matter. *Phys. Rev. D 7* (Feb. 1973), 953–964.

[71] Shabanova, T. V., and Shitov, Y. P. Properties of the linearly polarized radiation from PSR B0950+08. *Astron. Astrophys. 418* (Apr. 2004), 203–211.

[72] Shapiro, S. L., and Teukolsky, S. A. *Black holes, white dwarfs, and neutron stars: The physics of compact objects*. John Wiley & Sons, 1983.

[73] Thompson, C., and Duncan, R. C. Neutron star dynamos and the origins of pulsar magnetism. *Astrophys. J. 408* (May 1993), 194–217.

[74] Thompson, C., and Duncan, R. C. The soft gamma repeaters as very strongly magnetized neutron stars - i. radiative mechanism for outbursts. *MNRAS 275* (July 1995), 255–300.

[75] Urama, J. O., Link, B., and Weisberg, J. M. *Mon. Not. Roy. Astr. Soc. 370* (2006), L76.

[76] van der Horst, A. J., Connaughton, V., Kouveliotou, C., Göğüş, E., Kaneko, Y., Wachter, S., Briggs, M. S., Granot, J., Ramirez-Ruiz, E., Woods, P. M., Aptekar, R. L., Barthelmy, S. D., Cummings, J. R., Finger, M. H., Frederiks, D. D., Gehrels, N., Gelino, C. R., Gelino, D. M., Golenetskii, S., Hurley, K., Krimm, H. A., Mazets, E. P., McEnery, J. E., Meegan, C. A., Oleynik, P. P., Palmer, D. M., Pal'shin, V. D., Pe'er, A., Svinkin, D., Ulanov, M. V., van der Klis, M., von Kienlin, A., Watts, A. L., and Wilson-Hodge, C. A. Discovery of a New Soft Gamma Repeater: SGR J0418 + 5729. *Astrophys. J. Lett. 711* (Mar. 2010), L1–L6.

[77] van Riper, K. A. Neutron star thermal evolution. *ApJ 75* (Feb. 1991), 449–462.

[78] W. Baade, F. Z. Cosmic Rays from Super-novae. *Proc. Natl. Acad. Sci. 20* (Mar. 1934), 259–263.

[79] Wang, N., Manchester, R. N., Pace, R. T., Bailes, M., Kaspi, V. M., Stappers, B. W., and Lyne, A. G. Glitches in southern pulsars. *Mon. Not. R. Astron. Soc. 317* (Oct. 2000), 843–860.

[80] Zamfir, M., Cumming, A., and Galloway, D. K. Constraints on Neutron Star Mass and Radius in GS 1826-24 from Sub-Eddington X-Ray Bursts. *Astrophys. J. 749* (Apr. 2012), 69.

[81] Zavlin, V. E., and Pavlov, G. G. Modeling Neutron Star Atmospheres. In *Neutron Stars, Pulsars, and Supernova Remnants* (2002), W. Becker, H. Lesch, & J. Trümper, Ed., p. 263.

[82] Zavlin, V. E., Trümper, J., and Pavlov, G. G. X-Ray Emission from the Radio-quiet Neutron Star in Puppis A. *Astrophys. J. 525* (Nov. 1999), 959–967.